AN ABSTRACT OF THE THESIS OF

Anna L. Herring for the degree of Master of Science in Chemical Engineering presented on November 29, 2012

Title: Saturation, Morphology, and Topology of Nonwetting Phase Fluid in Bentheimer Sandstone; Application to Geologic Sequestration of Supercritical CO_2

Abstract approved:

Dorthe Wildenschild

This work examines the impact of a viscosity force parameter, fluid velocity, and a capillary force parameter, interfacial tension, on the saturation, morphology, and topology of NW fluid in Bentheimer sandstone after primary imbibition, drainage, and secondary imbibition. Brine and air (used as a proxy for supercritical CO_2) flow experiments were performed on 6 mm diameter Bentheimer cores and were quantified via imaging with x-ray computed microtomography (x-ray CMT), which allows for three dimensional, non-destructive, pore-scale analysis of the amount and distribution of NW phase fluid within the sandstone cores. It was found that trapped NW phase saturation decreases with increases in capillary number, average blob size decreases with increases in capillary number, and the number of NW blobs increases with increases in capillary number. In addition, it was found that NW phase trapping is dependent on initial NW phase connectivity within the porous medium; with more negative values of initial NW phase Euler number resulting in less trapping. We suggest that the Euler number-saturation and the capillary number-saturation relationships for a given medium should be taken into consideration when designing a CO_2 sequestration scenario.

Saturation, Morphology, and Topology of Nonwetting Phase Fluid in Bentheimer Sandstone; Application to Geologic Sequestration of Supercritical CO_2

by
Anna L. Herring

A THESIS

Submitted to

Oregon State University

In partial fulfillment of
the requirements for the
degree of

Master of Science

Presented November 29, 2012
Commencement June, 2013

Master of Science thesis of Anna L. Herring presented on November 29, 2012.

APPROVED:

Major Professor, representing Chemical Engineering

Head of the School of Chemical, Biological, and Environmental Engineering

Dean of the Graduate School

I understand that my thesis will become part of the permanent collection of Oregon State University libraries. My signature below authorizes release of my thesis to any reader upon request.

Anna L. Herring, Author

ACKNOWLEDGEMENTS

The author would like to express her sincere appreciation to Dorthe Wildenschild, for her patient and encouraging guidance; to her family, for their unwavering and staunch support; and to her friends, for being there for all the adventures.

TABLE OF CONTENTS

TABLE OF CONTENTS (Continued)

LIST OF FIGURES

LIST OF FIGURES (Continued)

LIST OF TABLES

1.0 Introduction

Energy production via the use of fossil fuels has resulted in the release and accumulation of substantial quantities of CO_2 in the atmosphere (IPCC, 1996). The prevalence and amount of coal in reserves throughout the world implies that despite concerns of excessive anthropogenic CO_2 emissions, coal will continue to be a large source of energy production in the future; this indicates that some form of emissions mitigation is necessary for coal-based power plants (Schrag, 2007). Geologic CO_2 sequestration has been suggested as a mitigation strategy with regards to energy production via coal power plants (IPCC, 2005) and short and long term security of storage of CO_2 in the subsurface is essential to a successful sequestration scheme.

Sequestration involves injection of supercritical CO_2 into a subsurface brine reservoir (considered to be a brine drainage process), and the subsequent upward travel of the buoyant CO_2 plume (during which the brine re-enters, or imbibes, back into the pore space). Ultimately, the CO_2 will dissolve into the brine ("dissolution trapping") and eventually precipitate to form carbonate minerals ("mineral trapping"). However, these dissolution and precipitation processes are estimated to occur on long timescales (on the order of hundreds to thousands of years) and a mobile CO_2 plume may exist in the subsurface until these reactions proceed to completion (IPCC, 2005). Entrapment of CO_2 via capillary forces within the pore structure of the rock ("capillary trapping") occurs on short time scales, and is more secure than trapping of a continuous CO_2 plume via a caprock ("hydrodynamic trapping") (IPCC, 2005).

In theory, maximization of capillary trapping can be accomplished via manipulation of injection scenarios. Parameters such as pressure,

temperature, and salinity conditions of the injection can be sought such that the fluid properties and thus interaction of the CO_2-brine system are most conducive to capillary trapping. Similarly, the flow rates of both the CO_2 injection and the subsequent brine injection/imbibition can be managed to provide favorable capillary trapping conditions.

This work investigates the changes in saturation, morphology, and topology of non-wetting phase as a function of fluid flow properties for a Bentheimer sandstone using air as a proxy fluid for CO_2. Drainage-imbibition experiments were performed in Bentheimer sandstone cores; and NW phase saturation was characterized using x-ray computed microtomography (x-ray CMT). Results suggest that a CO_2 injection can indeed be manipulated in order to maximize capillary-trapped NW phase and also facilitate entrapment of residual NW phase blobs with certain size and connectivity characteristics, which may be favorable with respect to other subsurface reactions (e.g. dissolution, re-mobilization). The results also highlight the importance of connectivity of the injected NW phase to a sequestration scheme.

2.0 Background

2.1 Multiphase Flow in Porous Media

The transport of CO_2 in the subsurface is a multi-phase transport problem, due to the immiscibility of CO_2 with brine. In two-phase fluid flow processes, there are three phases present: solid (the media matrix), wetting (W) phase, and non-wetting (NW) phase. The solid surface generally exhibits a strong affinity to one fluid phase over the other, this phase is termed the "wetting" phase as it preferentially wets the surface (a surface which does not have a strong affinity for either phase may be called "intermediate-wetting" or "mixed-wetting"). The strength of the affinity of the medium is measured by the contact angle that the fluid-fluid-solid interface forms on a flat surface. A hydrophilic medium is termed "water-wet" as it has a preference to be coated by water vs. the NW fluid. Analogously, a medium which is hydrophobic or has a high affinity for oil may be termed "oil-wet". Both the wettability state and the size of the medium influence the capillary pressure [mPa]; this describes the pressure difference due to the curvature between a wetting and non-wetting phase within a porous medium, and this relationship is characterized by the Young-Laplace equation:

$$P_c = P_{NW} - P_W = \sigma \left(\frac{1}{r_1} + \frac{1}{r_2}\right) cos\theta \qquad (1)$$

Here, σ is the interfacial tension (IFT) between the wetting (fluid 1) and non-wetting (fluid 2) phases [mN/m], r_1 and r_2 are the two principal radii of curvature [m^{-1}], and θ is the contact angle in degrees of the wetting fluid, as shown in Figure 1.

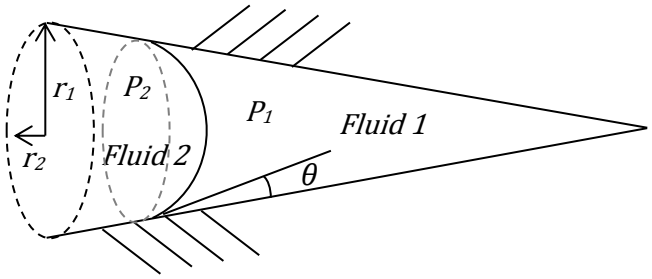

Figure 1. Interfacial curvatures leading to capillarity within a conical pore

Thus, smaller pore throats require a greater pressure difference to effect menisci movement. This relationship is described by the capillary pressure-saturation curve (Figure 2).

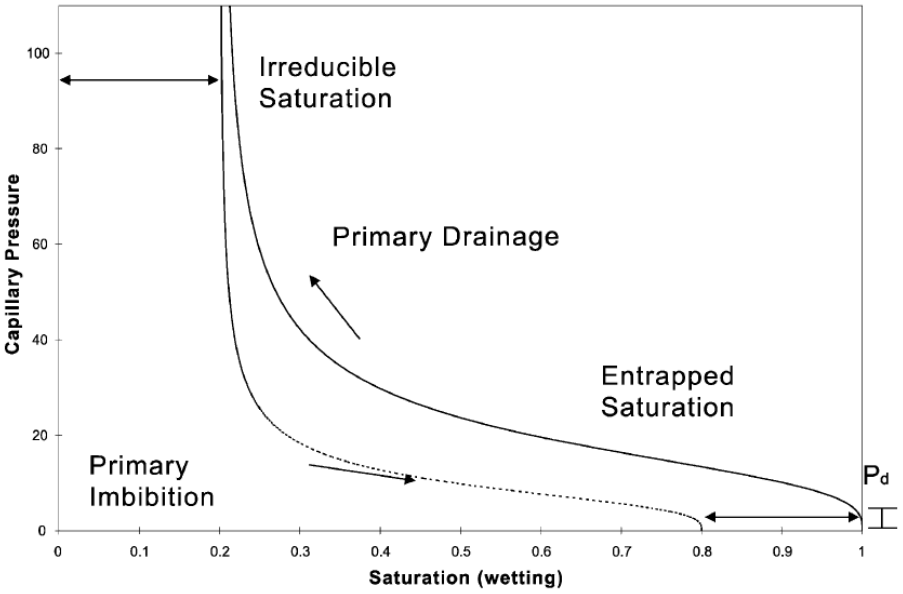

Figure 2. Example capillary pressure saturation curve (Van Geel and Roy, 2002)

As wetting fluid drains from full saturation, an initial pressure threshold must be overcome (the “air entry pressure”, labeled P_d on Figure 2), after which pores in theory drain according to the size of pore throats. A medium with a generally uniform pore size will have a relatively level draining slope at intermediate saturations (i.e. the same pressure is required to drain a large fraction of the pores). At low saturations, only the smallest pore throats remain wetting fluid-filled, and the pressure required to drain even relatively low volumes increases dramatically. This trend is reversed upon imbibition, but a lower pressure difference is required to imbibe wetting fluid back into the medium. This dependence on system history is termed “hysteresis”.

Depending on the extent to which the medium is imbibed or drained, non-wetting phase fluid bodies will be present in the larger pores rather than the smaller pores. This plays an important role in the permeability of the medium: wetting fluid flows easier through large pores and throats as compared to smaller ones, but the large throats are only filled at relatively high W phase saturation. Conversely, NW fluid may be present in larger pores at low saturation, but NW fluid flow is inhibited by low connectivity at low NW saturation. Thus, relative permeability curves take on shapes as shown in Figure 3: the medium exhibits a low permeability at low saturation for the respective phases, dramatically increasing as saturation of that phase increases and fills the larger throats and establish improved connectivity.

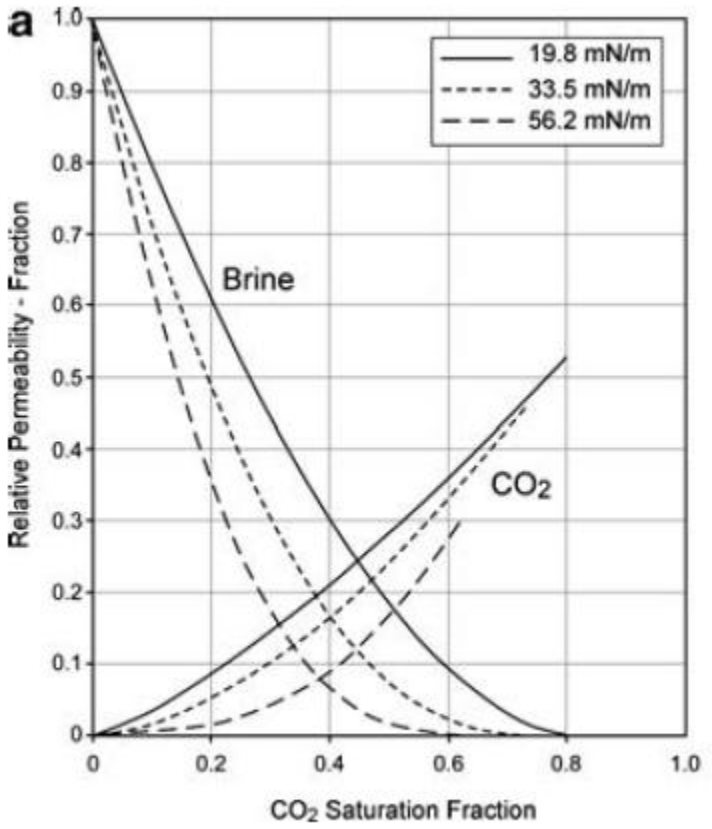

Figure 3. Relative permeability curves for CO_2 and brine at varying IFT (Bachu and Bennion, 2008)

Topological/morphological measures that describe fluid distribution in porous media include the coordination number (the number of pore throats connected to a pore body), the pore throat aspect ratio (the ratio of the size of a pore throat to the adjoining body), and grain size and shape. Further, the knowledge of the distribution of these parameters rather than average values is important to fully describe fluid flow. These measures can be difficult to define consistently due to resolution as well as media consistency and heterogeneity issues.

2.2 Fluid Properties

Multiphase fluid transport in porous media depends on the characteristics described above, but also on fluid properties (e.g. viscosity, interfacial tension, density) and engineering parameters (e.g. flow rate of a pumping scheme). At depths suggested for CO_2 storage (on the order of thousands of feet deep), reservoir pressure and temperature conditions are beyond the critical point of CO_2 (73.8 bar and 31.1 ^{o}C). Bachu and Bennion (2008) have shown that super-critical CO_2 (s.c. CO_2) has a range in IFT from approximately 20 mN/m to 50 mN/m with changes in brine salinity, temperature, and pressure. Similarly, viscosity and density can range an order of magnitude with temperature and pressure (Bachu, 2003). This variation in physical parameters of CO_2 implies that the temperature and pressure of the CO_2 injection and subsequent brine imbibition can be optimized to maximize residual CO_2 saturation and allow for favorable morphological and topological characteristics.

2.2.1 Dimensionless Ratios Describing Fluids and Flow

To facilitate characterization of flow over a range of properties, the experiments discussed in this work are characterized by the following three dimensionless ratios: Capillary Number (Ca), Bond Number (Bo), and Mobility Ratio (M).

The capillary number has several definitions depending on the intended application (Chatzis and Morrow, 1984, Yadali Jamaloei et al., 2012), but has traditionally been defined from an oil extraction standpoint. In general, the capillary number describes the balance between viscous forces and capillary forces with respect to the invading fluid (as opposed to the defending fluid). Thus, in this work, Ca is defined as:

$$\mathrm{Ca} = \frac{\mu_{INV} v_{INV}}{\sigma} = \frac{\mu_{INV} \frac{Q_{INV}}{A\eta}}{\sigma} \quad (1)$$

where μ_{INV} is the invading phase viscosity [mPa·s] and v_{INV} is the invading phase velocity [m/s] which is calculated as the volumetric flow rate Q [m^3/s] divided by the cross-sectional area A [m^2] of the porous medium and the porosity η [-]. We assume that the invading phase velocity and the defending phase velocity are equal, but in order to fully describe both fluids, the viscosity of both phases needs to be considered. Thus, the Mobility Ratio (M) is utilized, as defined below, following Lenormand et al. (1988):

$$\mathrm{M} = \frac{\mu_{INV}}{\mu_{DEF}} \quad (2)$$

where μ_{DEF} is the viscosity of the defending fluid [mPa·s].

The fluid pair (KI brine and air) used in this work was chosen to utilize ambient conditions while remaining applicable to the flow regimes relevant to supercritical CO_2. See Table 1, which shows relevant properties of the proxy fluid pair (air- KI brine with surfactant) as compared to those of supercritical CO_2. Similarly, Figure 1, after Lenormand et al. (1988), shows the relative location within the so-called Flow Regime Phase Diagram of the supercritical CO_2-brine system during the trapping stage (i.e. the imbibition process following CO_2 injection) and the experiments conducted for this work.

Table 1. Fluid Properties

	KI Brine (with surfactant)	**Air**	**s.c.CO_2** (approximate range)
IFT with brine (mN/m)	-	30 - 72	20 – 50[a]
μ (mPa-s)	1.13	0.018	0.025 – 0.15[b]
Density (kg/m^3)	1080	1.2	465 – 900[b]

a) Bachu and Bennion, 2008
b) Bachu, 2003

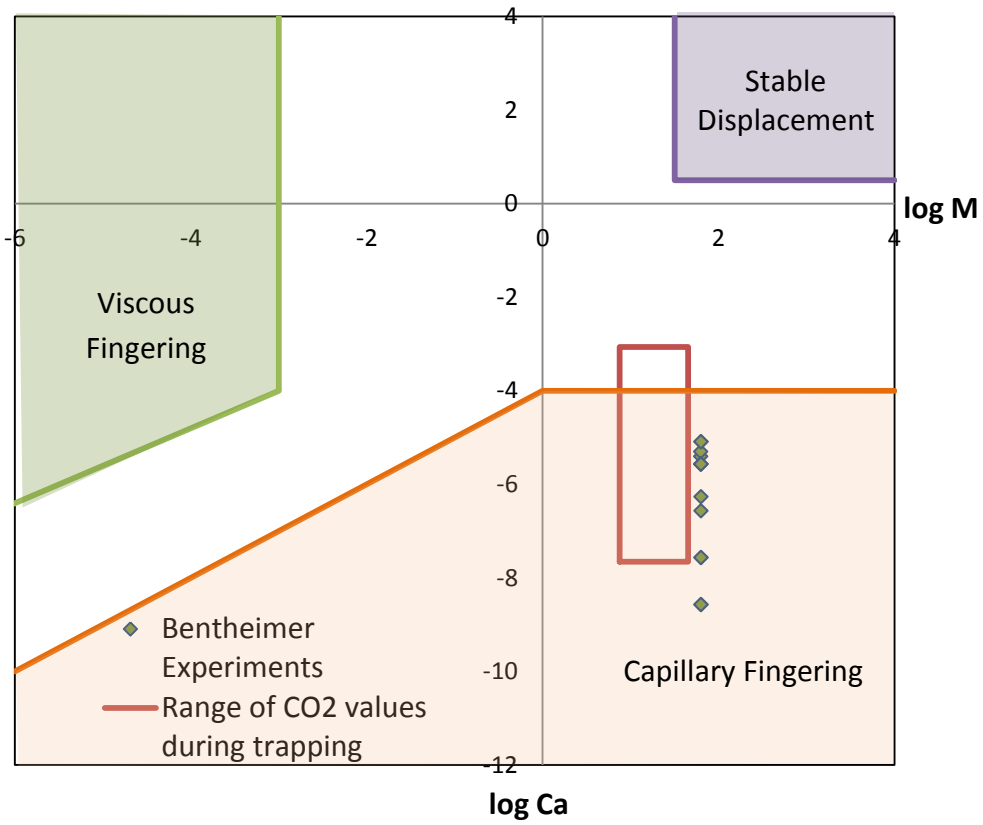

Figure 4. Flow regime phase diagram as developed by Lenormand et al. (1988)

Figure 4 demonstrates the impact of both invading and defending phase capillary and viscous forces on the system. The flow regimes shown have distinct characteristics: stable displacement presents a relatively uniform, flat front; viscous fingering displays tree-like fingers which grow outward as the flow moves away from the injection point; and capillary fingering exhibits fingers which grow in all directions (even backwards, towards the injection point), forming loops which trap the displaced fluid (Lenormand et al., 1988). This model describes multiphase flow in 2D micromodels; however, in a 3D system, the gravity force must also be included. To that end, we define the Bond number as the ratio of gravity forces to capillary forces:

$$\mathrm{Bo} = \frac{\Delta\rho \cdot g \cdot d^2}{\sigma} \qquad (3)$$

where: $\Delta\rho$ is the density difference between the two fluids [kg/m^3], g is the acceleration of gravity [m/s^2], and d is the representative length scale [m]. Here, for ease of comparison with other works, d is defined as the average grain size (or equivalent grain size for a micromodel). For convenience, the inverse Bond number will be used more frequently here, representing the capillary to gravity force balance:

$$\mathrm{Bo}^{-1} = \frac{\sigma}{\Delta\rho \cdot g \cdot d^2} \qquad (4)$$

Note that while Ca and M are dependent upon whether the system is undergoing imbibition or drainage, Bo and Bo^{-1} are constant for a given fluid pair-porous medium system.

Incorporation of this third dimensionless ratio allows for a 3D characterization of flow regimes studied in this work based on a force balance perspective (Figure 4, modified after Polak et al. (2011)). Locations of glass bead and angular sand experiments (See Section 5.3) are included for comparison.

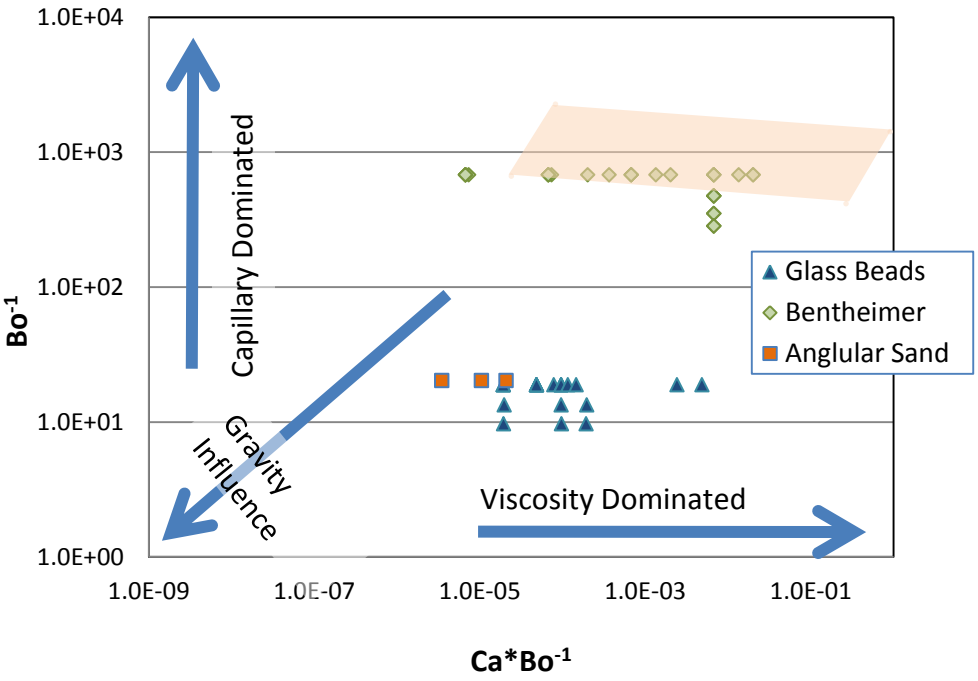

Figure 5. Pore scale force balance

As shown, the x-axis represents the ratio of viscous to gravity forces, signifying the transition from gravity to viscosity dominated flow:

$$\mathrm{Ca}\cdot\mathrm{Bo}^{-1} = \frac{Viscosity}{Capillarity}\frac{Capillarity}{Gravity} = \frac{Viscosity}{Gravity} = \frac{\mu_{INV} v_{INV}}{\Delta\rho \cdot g \cdot d^2} \qquad (5)$$

Similarly, the y-axis represents the transition from gravity domination to capillary domination. Thus, near the origin, gravity forces dominate, while away from the origin capillary and/or viscosity become more important.

Note, however, that the non-wetting phase viscosity is not included in this model, which may lead to conflicting results, especially in a viscosity-dominated regime. Also note that medium topology and morphology (coordination number, pore-throat aspect ratio) and other features (porosity, consolidated vs. unconsolidated, wettability) which may also be important to multiphase fluid flow are not well-represented by this model.

Figure 5 demonstrates the location of this work within a pore-scale force balance. The conditions of relevance to a supercritical CO_2 trapping process are indicated by the orange box. From Figures 4 and 5 it is shown that the results of this work are applicable to the supercritical CO_2- brine system, both from a 2D fluid characterization standpoint and a 3D force balance point of view.

2.3 Quantitative Measures

2.3.1 NW Phase Residual Saturation

Considerable research has been devoted to how to control the saturation of residual NW phase in a matrix, i.e. NW phase present after a waterflood or imbibition process has occurred. In this case, saturation is quantified as the fraction of total pore volume occupied by nonwetting fluid. Furthermore, “trapping” indicates residual saturation (NW phase present after the final imbibition process) normalized by initial saturation (NW phase present after primary drainage). This is an important parameter in oil recovery operations and NAPL remediation in the subsurface, as well as for CO_2 sequestration applications. However, in contrast to oil recovery and NAPL removal operations, the goal of a CO_2 sequestration scenario is to maximize NW phase trapping.

2.3.2 Morphology of NW Phase

The morphology of the non-wetting phase is characterized by measures such as the size of NW phase elements ("blobs"), their shapes, and the number of blobs present in the sample. In this work, the average blob volume is used as a metric to give an indication of the size of the individual fluid elements within the porous medium, and the blob number is normalized by the saturation of the sample. This is done because a sample with higher residual NW phase saturation is expected to have more blobs present, so in order to determine the individual effects of flow rate and IFT on morphology, blob numbers are divided by their respective saturation values. The volume and number of individual blobs is important for dissolution and remobilization processes.

2.3.3 Topology of NW Phase

Topology describes the "connectedness" of a phase. Topological studies involve quantification of object properties which are conserved under continuous deformations (e.g. folding or stretching) but not conserved under discontinuous deformations (e.g. breaking or joining).

For our purposes, the Euler number (χ) is used to characterize the topology of the NW phase. The Euler number is defined as

$$\chi = \beta_0 - \beta_1 + \beta_2 \qquad (6)$$

Where β_0 is the zeroth Betti Number, referring to the number of distinct fluid elements in the volume; β_1 is the first Betti number, which refers to the number of "handles" or redundant loops present in the structure of the fluid element; and β_2 is the second Betti Number, indicating the number of "holes" in the element. A visual representation of the three Betti numbers is shown in

Figure 6. In general, as χ decreases, the fluid element is considered to become more connected, and subsequently, more "complex".

(a) **(b)** **(c)**

Figure 6. Betti Number and Euler Number examples.

(a) Two distinct bodies: $\beta_0 = 2, \beta_1 = 0, \beta_2 = 0$ $\chi = 2 - 0 + 0 = 2$
(b) One distinct body with a loop: $\beta_0 = 1, \beta_1 = 1, \beta_2 = 0$ $\chi = 1 - 1 + 0 = 0$
(c) One distinct hollow body: $\beta_0 = 1, \beta_1 = 0, \beta_2 = 1$ $\chi = 1 - 0 + 1 = 2$

Considered all together, the grouping of (a), (b), and (c) results in $\beta_0 = 4$, $\beta_1 = 1$, and $\beta_2 = 1$; with a total Euler Number of $\chi = 4 - 1 + 1 = 4$ (i.e. the sum of the individual Euler Numbers).

For a low density non-wetting fluid in a porous medium (e.g. air, in this study), β_2 is unrealistic to consider, since it would imply the presence of a suspended wetting fluid or solid element completely surrounded by air. So, for this work, the Euler number is simply considered to be

$$\chi = \beta_0 - \beta_1 \qquad (7)$$

Euler numbers reported in this work are the total Euler numbers of all the NW phase fluid elements within the volume (i.e. each image volume is presented with a single χ measurement for the entire volume).

2.4 X-Ray Computed Microtomography

These experiments were quantified with the use of x-ray computed microtomography (x-ray CMT), a non-destructive method of 3D sample analysis. X-ray microtomography has been utilized in geology, hydrology, and

oil recovery work in order to visualize and characterize the internal 3-dimensional structure of porous media (Youssef et al., 2010, Setiawan et al., 2012, Wildenschild et al., 2002, Silin et al., 2011, Ketcham and Carlson, 2001, Al-Raoush and Willson, 2005, Blunt et al., 2012). For a thorough overview of the use of x-ray CMT in fluid flow experiments, the reader is referred to Wildenschild and Sheppard (2012). A brief theoretical introduction follows here.

The basis of x-ray imaging is the Beer -Lambert law, which states that an x-ray beam is attenuated from the incident intensity, I_0 , to the final intensity, I, after passing through a sample of thickness D [L] with linear attenuation coefficient μ [L^{-1}]:

$$I = I_0 \exp(-\mu D) \qquad (8)$$

For a sample containing multiple phases (i.e. solid, water, and gas phases in this study), equation 8 can be modified as:

$$I = I_0 e^{-[(1-\theta)\mu_s \rho_s D + \theta S_w \mu_w \rho_w D + \theta(1-S_w)\mu_g \rho_g D]} \qquad (9)$$

where subscripts s, w, and g represent solid, water, and gas respectively; ρ is substance density [ML^{-3}], θ is the sample porosity, and S_w is the water saturation. In general, the x-ray attenuation by the gas phase is assumed to be negligible, resulting in equation 10:

$$I = I_0 \exp(-[(1-\theta)\mu_s \rho_s D + \theta S_w \mu_w \rho_w D]) \qquad (10)$$

The linear attenuation coefficient for any given material is a function of material density, atomic number, atomic weight, and the energy of the x-ray beam. The goal of this and similar studies is to choose contrast agents (e.g. potassium iodide in the wetting fluid, in this case) and x-ray energies such

that the different phases have distinct linear attenuation coefficients; this allows separation of the materials during processing of the data.

X-ray tomography consists of the collection of sequential, contiguous radiographs, taken in minute increments 360^{o} around the sample. The individual images are compiled together during processing (Section 4.3) to resolve details in three dimensions. Microtomography is a form of tomography capable of resolving features of the sample on the micron scale. Resolution is described by voxel size; a 3D voxel is analogous to a 2D pixel.

The basic components of a tomography system include the x-ray source, the stage upon which the sample is placed, and the camera which collects the images (Figure 7).

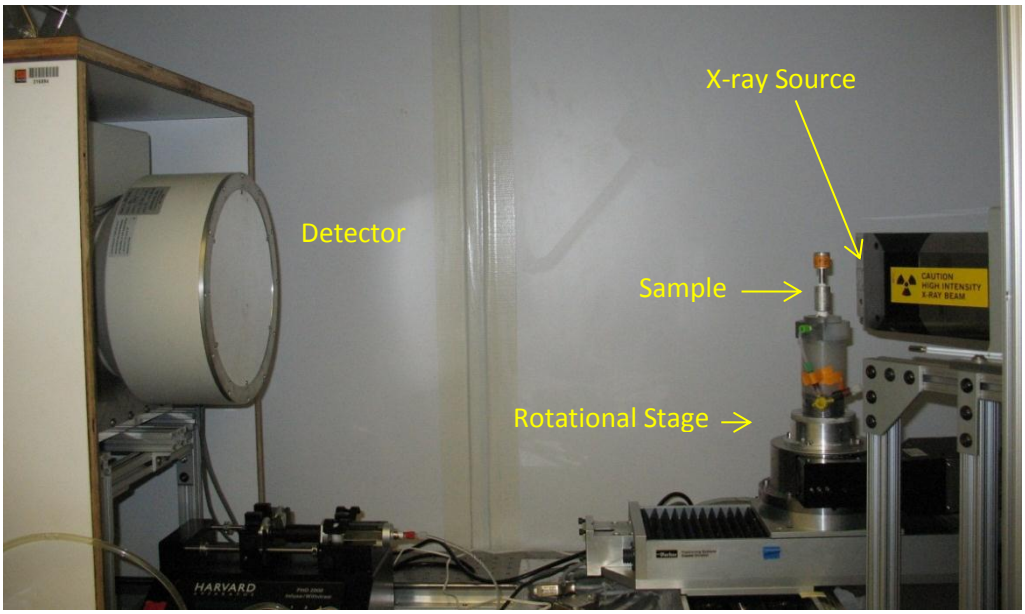

Figure 7. "Bench top" x-ray tomographic system, courtesy of MIME, Oregon State University

3.0 Current State of Residual Trapping Research and Characterization

A number of NW phase trapping studies have been conducted previously, and will be discussed in the following. Figure 8 shows the location of a number of existing multiphase flow studies overlaid onto the pore scale force balance diagram introduced earlier. Conditions relevant to supercritical CO_2 trapping in sandstone reservoirs are indicated by the orange box. Table 2 lists the type of experiments and major results of the references shown in Figure 8, as well as some additional studies (spontaneous imbibition/drainage studies and micromodel studies are not included on Figure 8). These experiments are discussed in the following in the context of force balance, total residual NW phase saturation (3.1), NW phase morphology (3.2), and topology (3.3).

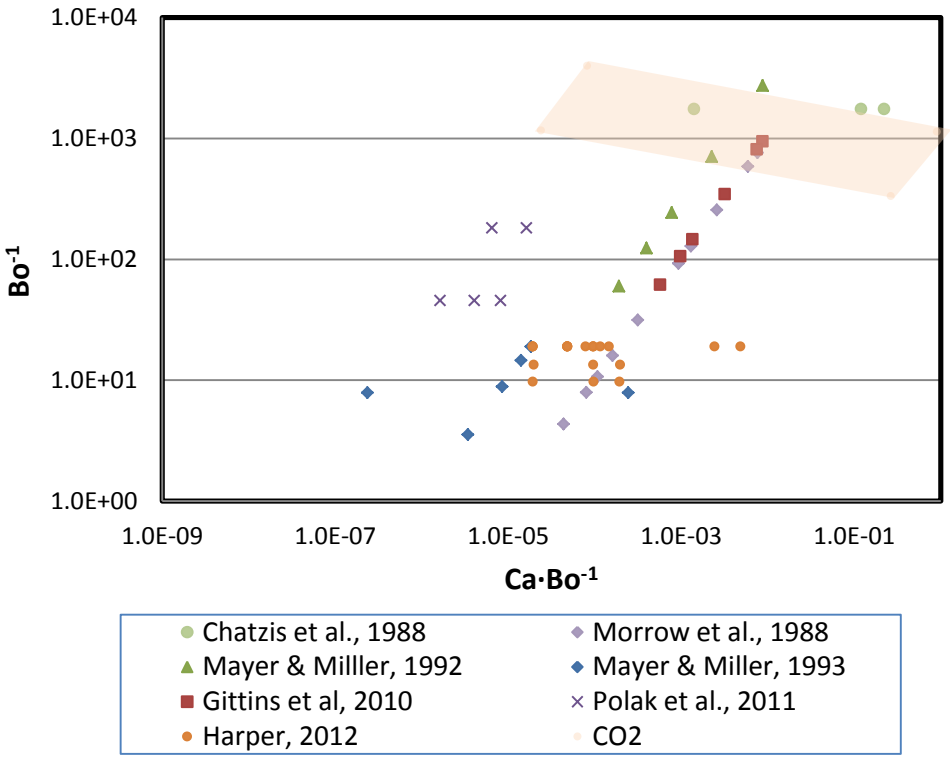

Figure 8. Previous works and pore scale force balance

Table 2. Previous Research

	Reference	Dimension	Flow Notes	Media	Experimental Range of Dimensionless Parameters: Ca	M	Bo^{-1}	Dominant Force	Other notes
	Herring, 2012 (this work)	3-D	Vertical Flow	Sansdstone	$10^{-8.6}$ $10^{-4.8}$	$10^{0.25}$	$10^{2.5}$ $10^{2.8}$	Capillary/Viscous	
Fluid Front Regime									
	Polak et al., 2011	pseudo 2-D	Vertical Flow	Glass Beads	$10^{-7.4}$ $10^{-6.7}$	$10^{-2.1}$	$10^{1.7}$ $10^{2.3}$	Capillary/Viscous/Gravity	
	Lenormand et al., 1988	2-D	Lateral Flow	Micromodel	$10^{-9.4}$ $10^{-0.9}$	$10^{-4.7}$ $10^{2.9}$	NA	Capillary/Viscous	
	Wang et al., 2012	2-D	Lateral Flow	Micromodel	$10^{-7.6}$ $10^{-4.7}$	$10^{1.25}$	NA	Capillary/Viscous	
Saturation									
	Morrow et al., 1988	3-D	Vertical Flow	Glass Beads	$10^{-5.3}$ 10^{-2}	NA	$10^{0.6}$ $10^{2.9}$	Capillary/Gravity	
	Chatzis et al., 1988	3-D	Lateral Flow	Sandstone	$10^{-6.1}$ $10^{-3.9}$	$10^{0.12}$	$10^{3.2}$	Capillary /Viscous	
	Schechter et al., 1994	3-D	Spontaneous Imbibition	Limestone, Sandstone	NA	$10^{0.32}$ $10^{0.81}$	$10^{0.33}$ $10^{3.7}$	Capillary/Gravity	S_R decreases as Bo^{-1} decreases
	Gittins et al., 2010	3-D	Lateral Flow	Unconsolidated Sand	$10^{-5.0}$	$10^{0.27}$	$10^{1.8}$ $10^{3.0}$	none identified	grain size (i.e. Gravity) not important
	Mayer and Miller, 1992	3-D	Vertical Flow	Glass Beads	$10^{-3.5}$	$10^{0.12}$	$10^{1.8}$ $10^{3.4}$	none identified	grain size (i.e. Gravity) not important
	Harper et al., 2012	3-D	Vertical Flow	Glass Beads	10^{-6} $10^{-3.6}$	$10^{-0.63}$ $10^{2.34}$	10 $10^{1.45}$	Viscous	
Morphology									
	Chatzis et al., 1988	3-D	Lateral Flow	Sandstone	$10^{-6.1}$ $10^{-3.9}$	$10^{0.12}$	$10^{3.2}$	Capillary /Viscous	velocity dominates morphology
	Mayer and Miller, 1992	3-D	Vertical Flow	Glass Beads	$10^{-3.5}$	$10^{0.12}$	$10^{1.8}$ $10^{3.4}$	Gravity	S_R remains unaffected by grain size
	Mayer and Miller, 1993	pseudo 2-D	Lateral Flow, but vertical orientation of model	Glass Beads	$10^{-7.5}$ $10^{-4.5}$	$10^{-0.24}$ $10^{0.44}$	$10^{0.6}$ $10^{1.3}$	Gravity	NW viscosity not taken into account
	Chao et al, 2000	3-D	Spontaneous drainage	Glass Beads	NA	$10^{-0.57}$	$10^{-1.4}$ $10^{0.4}$	Capillary	IFT dominates morphology
Topology									
	Wardlaw and Yu, 1988	2-D	Lateral Flow	Micromodel	$10^{-4.3}$	$10^{-1.9}$ $10^{0.17}$	NA		Fluid topology important for systems with low aspect ratio, uniform pore sizes, and high initial NW saturation

Following Polak et al. (2011), we suggest that the relative location of a system within the pore-scale force balance is responsible for which parameters are dominant in the system. In their study, Polak and colleagues demonstrated the interplay of all three capillary, viscous, and gravity forces resulting in a figure very similar to that shown in Figure 8; however, we have modified their original plot in order to more easily accommodate comparison of a wider range of experimental studies.

Additional studies have also shown the transition between different flow regimes and front morphologies obtained by varying combinations of Ca, M, and Bo (Heiß et al., 2011, Lenormand et al., 1988, Wang et al., 2012, Schechter et al., 1994, Hatiboglu and Babadagli, 2010, Vizika et al., 1994, Shen et al., 2010).

3.1 Total Residual NW Saturation

It is generally accepted that absolute amount of trapped NW phase for a given medium is correlated with Ca, with residual NW phase remaining relatively constant at lower Ca values and decreasing sharply at some threshold or “critical” Capillary number (Figure 9, Cense and Berg (2009)).

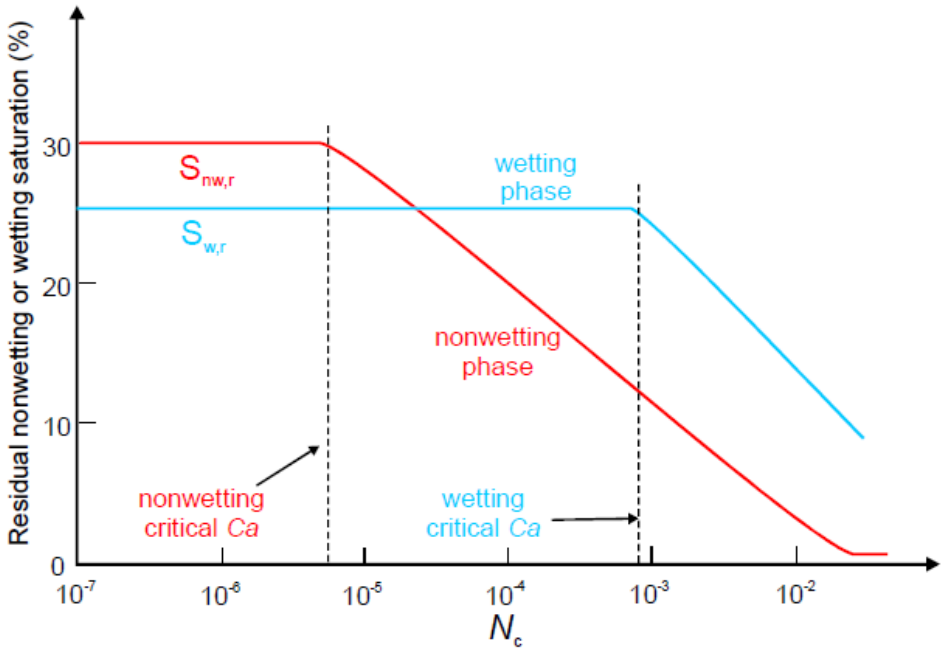

Figure 9. Capillary de-saturation curve (Cense and Berg, 2009)

This relationship has been demonstrated with experimental work (Suekane et al., 2010, Chatzis et al., 1988, Morrow et al., 1988) as well as modeling results (Hughes and Blunt, 2000, Nguyen et al., 2006).

This desaturation relationship is not purely a function of Ca, however, as the curves can shift due to changes in NW fluid properties (Figure 10, Ding and Kantaz (2007)) or medium properties (Figure 11, Nguyen, Sheppard et al . (2006)):

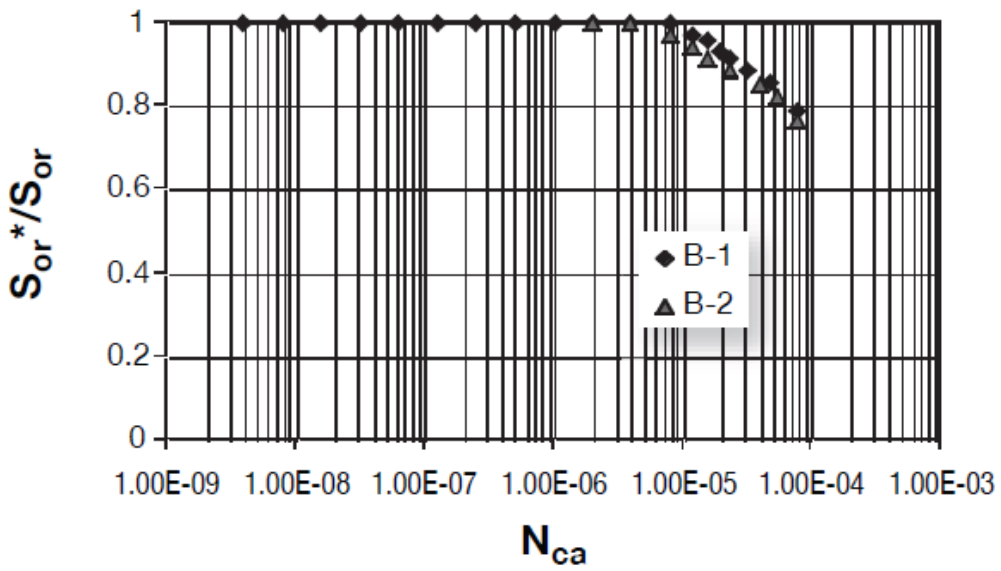

(a)

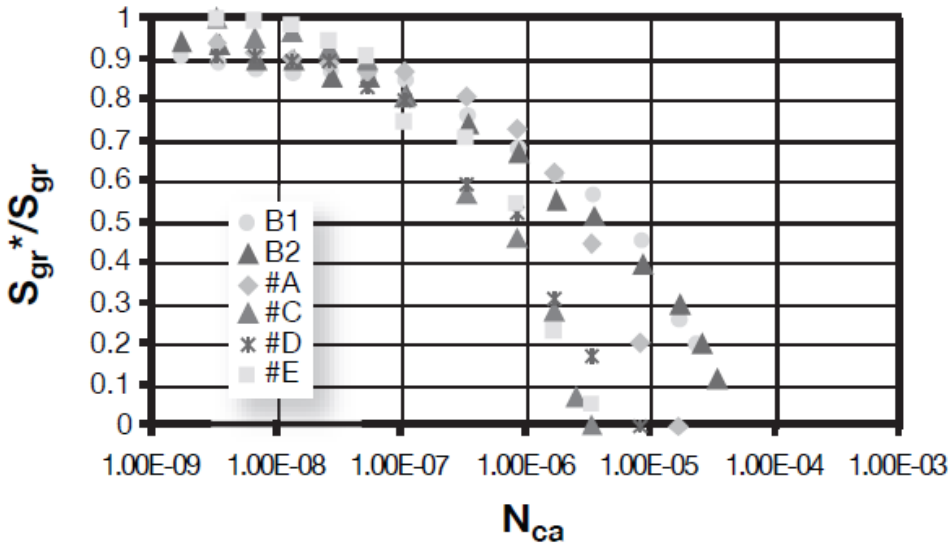

(b)

Figure 10. Residual saturation trends for (a) oil-water and (b) gas-water experiments (Ding and Kantzas, 2007)

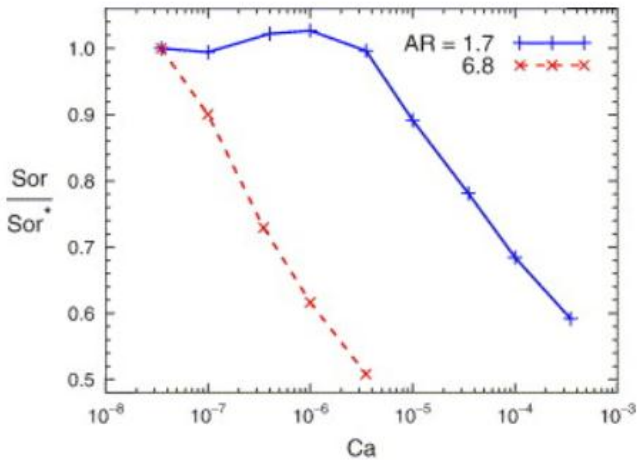

Figure 11. Residual saturation dependence on capillary number for low and high aspect ratio cases (Nguyen et al, 2006)

Similarly, trapped saturations show trends with respect to Bo^{-1} as well. Schechter and Zhou et al. (1994) demonstrated decreased residual saturation at the lowest Bo^{-1} during spontaneous imbibition via the manipulation of IFT and density of fluids. Morrow et al. (1988) investigated NW saturation in different sized glass bead cores and found that trapped residual saturation was correlated with inverse bond number as well as inverse capillary number. This is supported by Figure 8, which shows that Morrow et al.'s experiments range from the capillary/viscous regime to the gravity controlled regime.

In contrast, Mayer and Miller (1992) looked at the impact of bead size (a gravity force parameter) on residual NW saturation in glass bead cores and found no relationship. Gittins et al. (2010) looked at six different unconsolidated sand packs and found that porosity was the main factor influencing trapped NW saturation (with higher porosity leading to less trapping); while other media properties such as pore scale coordination number, pore-throat aspect, grain size, and grain shape had little or no effect

on the total amount of NW phase residual saturation. We suggest that this is due to the fact that the sand packs and glass bead cores used in these experiments are located in the capillary-viscosity dominated regime, so changing a gravity force parameter (i.e. grain size) should not be expected to have large effect on residual saturation.

Another factor influencing residual saturation is the initial saturation of NW fluid in the medium prior to imbibition and thus the trapping process (Al Mansoori et al., 2009). This relationship is characterized by a large initial increase in trapping with increasing initial saturation, with a more gradual slope above an initial saturation of approximately 40% (Figure 12, from Al Mansoori et al. (2009)).

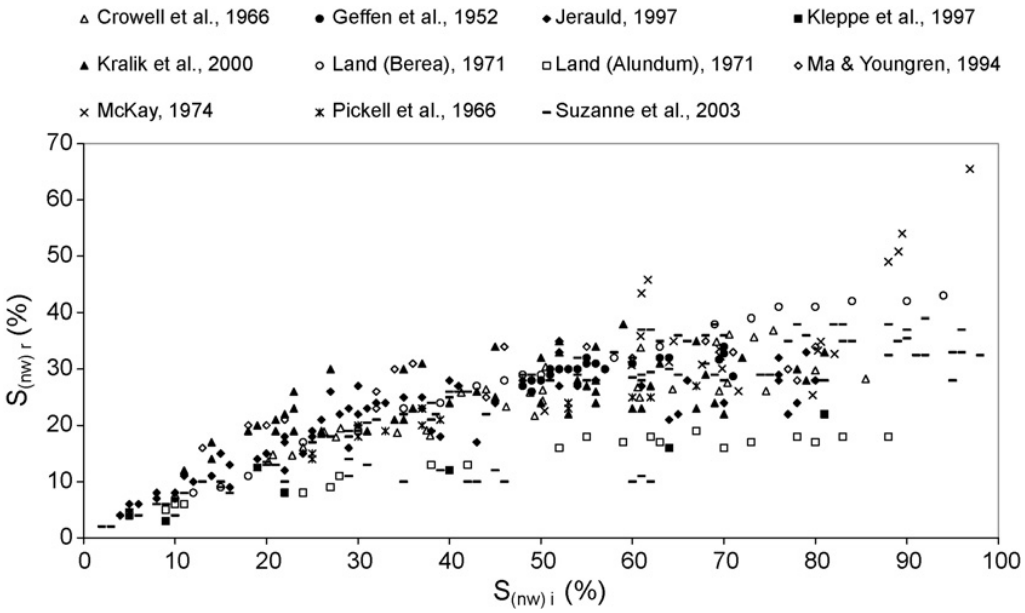

Figure 12. Residual trapping as a function of initial NW saturation (Al Mansoori et al., 2009)

3.2 NW Phase Morphology

Morphological characterization of NW phase in porous media has been reported in a couple of studies previously: Mayer and Miller (1993) studied a glass bead system with wetting fluid and multiple DNAPLs and found that NW blob length and the square root of blob surface area was much more dependent on Bo than Ca. Similarly, in a different set of experiments, Mayer and Miller (1992) found that while total residual saturation was independent of Bo, NW blob sizes were dependent on porous medium size in glass bead experiments; finding that blob length and volume increase with bead size. These works suggest that for the glass bead system, gravity has a large impact on morphology (if not saturation), even as the system approaches a more capillary-viscous dominant regime. Other works have shown a greater dependence on fluid properties; e.g. Chao et al. (2000) performed spontaneous flow column experiments in glass beads containing water plus surfactant and Soltrol 220, and found smaller ganglia and thinner fingers of NW phase at lower IFT, with no dependence on bead size. Chatzis et al. (1988) reported that NW blob size decreased with increasing Ca (as modified by fluid velocity) for oil and water experiments in sandstone cores. These results suggest that it is possible that the pore scale force balance plays a role in determining NW phase *morphology*; however, the boundaries of force relevance may be shifted from those relevant to *total residual saturation* determination.

3.3 NW Phase Topology

Many works have utilized topological measures to characterize the internal structure of porous media and relevant media properties for fluid flow (Wardlaw, 1986, Sok et al., 2002, Vogel, 2002, Arns et al., 2004, Mahmud et al., 2007, Vogel et al., 2010). Additional work has been done to try to identify

specific geometric properties of media which lead to increased NW residual trapping. For example, Chatzis et al. (1983) looked at several different experimental systems (glass bead packs, 2D micromodels, and Berea sandstone) and concluded that residual NW phase distribution and trapping type (i.e. snap-off vs. bypassing) is dependent on pore-throat aspect ratio, with secondary consideration given to coordination number. In support of this conclusion, Al-Raoush and Willson (2005)utilized tomography to identify residual NW phase within a glass bead pack and found that NW phase was trapped primarily in the pore bodies with the highest aspect ratio and highest coordination number.

However, there are relatively few works that study the topology of the *NW fluid phase* within a porous medium itself. In one of the few studies to address this topic, Wardlaw and Yu (1988), used 2-D micromodels to investigate NW phase topology and found that more highly connected initial NW phase leads to a decrease in residual saturation. Wardlaw and Yu also state that the effect of NW phase topology is more important for media with low pore-throat aspect ratio, and uniform pore size distributions. This indicates that different injection schemes (e.g. water alternating gas, or WAG) resulting in different fluid topologies may have varying efficiencies for different media.

To our knowledge, this is the first research studying the 3D topology of a fluid phase within a porous medium as characterized by the Euler number.

3.4 Research Goals

As shown in Figure 8, the trapping of supercritical CO_2 in a brine wetting phase (highlighted by the orange box) is a capillary-viscous force dominated process (assuming injection into a sandstone reservoir), so this research is

focused at studying the effects of capillary and viscous force parameters. Due to the inherent difficulty involved in changing the viscosity of our NW phase proxy fluid (air) without modifying other relevant parameters (IFT, density); viscous forces are modified by altering the velocity of flow through the column. The capillary force is modified by changing the IFT of the air-brine interface via the addition of surfactants. This research utilizes x-ray CMT to compliment previous experimental results and to investigate the effects of velocity and IFT on the total saturation, morphology, and topology of NW phase.

4.0 Methods

4.1 Experimental Procedure

The Bentheimer rock samples are cored from larger pieces of sandstone, which originate from the same formation and are expected to have similar pore size distributions, permeabilities, porosities, and aspect ratios. All cores have a diameter of 6 mm; core lengths range from 28-45 mm. Cores are wrapped with a thin layer of Teflon tape and epoxied into aluminum core holders (Figure 13).

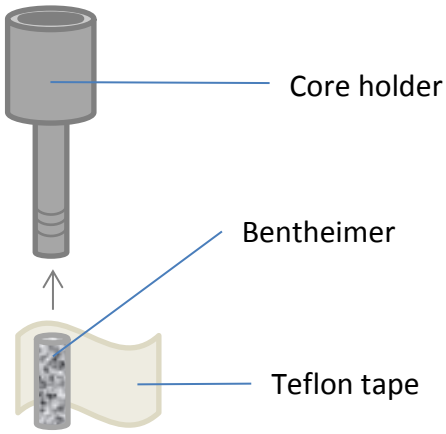

Figure 13. Core holder preparation

A Harvard PhD syringe pump is used to precisely control volumes and flow rates of fluids. A low-range and a high-range pressure transducer are connected in parallel to allow for verification of pressure measurements and allow for measurement of a wide range of pressure values. The low-range transducer provides fine pressure measurements at low pressure and is disconnected at higher pressures to prevent failure of the pressure transducer membrane, at which point the high-range transducer is utilized. A schematic of the experimental set-up is shown in Figure 14. The flow rates and fluid properties of the experiments are shown in Table 3.

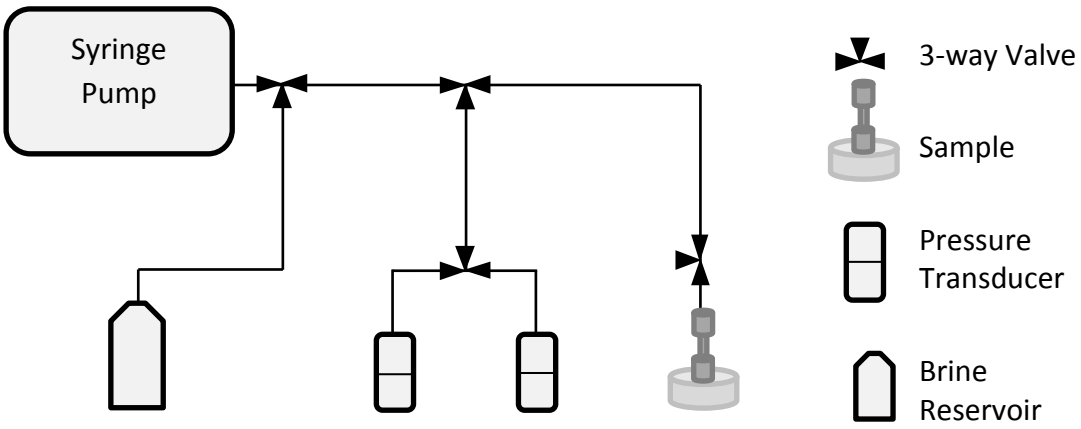

Figure 14. Experimental set-up schematic

Table 3. Experimental parameters

	Surfactant Concentration (ppm)	IFT (mN/m)	Imbibition Flow Rate (ml/min)	Ca
Velocity Experiments				
Brine- Air	0	72.8	0.0003 – 0.9	$10^{-8.6}$ - $10^{-5.1}$
IFT Experiments				
Brine- Air	0	72.8	0.3	$10^{-5.6}$
Triton[a]-Air	13	44.9	0.3	$10^{-5.4}$
FC-4430[b]-Air	200	33.2	0.3	$10^{-5.2}$

[a]Sigma-Aldrich Triton™ X-100
[b]3M™ Novec™ Fluorosurfactant FC-4430

During an experiment, the rock core is first flushed with gaseous CO_2 for 30 minutes at a pressure of approximately 15 psi to attempt to replace all the air-filled pores with gaseous CO_2; this increases the dissolution of the gas within gas-filled pores and results in a higher brine saturation at the initial stage of the flow experiment. Two layers of hydrophilic nylon membrane with 1.2 micron pore size are used at the base of the sample stage; this prevents

NW fluid from entering the brine line. Two layers are used to prevent abrasion-puncture of the membrane when the rock core is attached to the base. The complete core holder assembly is shown in Figure 15. The gaseous CO_2-filled rock core is attached to the base and flushed with 10 pore volumes of brine at a high flow rate (1 ml/min, corresponding to Ca ≈ 10^{-5}); the system is then allowed to equilibrate to enhance dissolution of the pore space CO_2, and then another 10 pore volume brine flush is conducted to remove any acidified brine from the sandstone core.

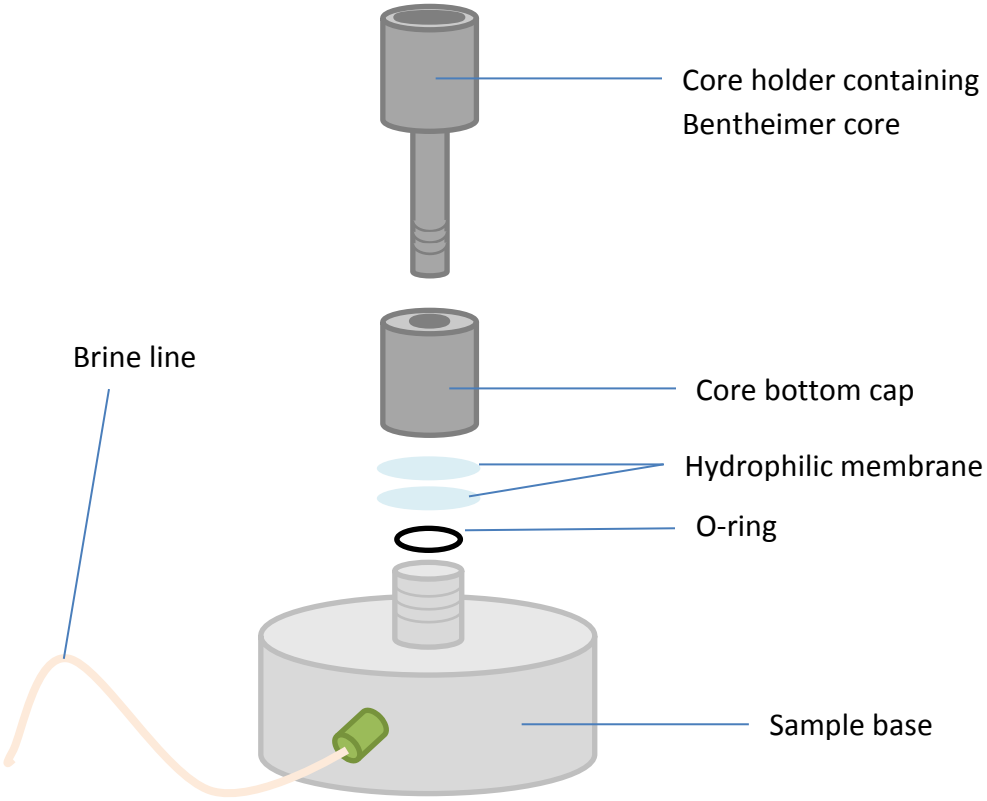

Figure 15. Core holder assembly

At this point, the sandstone system is assumed to represent a fully saturated state; however, as shown in Section 5.1, there is still some low residual

amount of gas after this process (≤ 6% of the pore space). A scan is acquired to record the original NW phase saturation ($\mathbf{S_0}$). Upon completion of the S_0 scan, the core is drained at a low flow rate (0.3 µl/min, Ca ≈ $10^{-8.6}$) to a specified volume equal to approximately 90% of the core pore volume. Pressure is carefully monitored during this process to ensure there are no leaks or membrane failure. Upon completion of drainage, another scan is acquired of this NW phase initial saturation ($\mathbf{S_I}$). Finally, wetting fluid is re-imbibed into the core at variable flow rate until brine appears and covers the top of the core, and pressure is monitored here to ensure appropriate forced-imbibition response. A final scan is acquired of the core at this residual NW phase saturation ($\mathbf{S_R}$). The core is cleaned by flushing with approximately 100 pore volumes of deionized water and either vacuum-dried or oven-dried.

4.2 X-ray Computed Microtomography

The scanner used for these experiments utilizes a cone-beam Focus FXE-160.20 x-ray source; and projections are collected with a 2448 X 2048 pixel (16-bit) CCD camera. All scans were conducted at 110 kV and 71 µA. Each scan consisted of 360^{o} of rotation in 1400 increments and used 6 averages per increment, resulting in scan times of 2.25 to 3 hours. Resolution under these settings is approximately 10 µm.

Other data presented in Section 5.3 (glass beads, angular sand) have been collected using different resolutions, x-ray generation methods, and beam types. Considerable effort has been made to ensure the quantitative results presented here are comparable despite these differences in data collection.

Access to the x-ray scanner was provided by Dr. Brian Bay in the School of Mechanical, Industrial, and Manufacturing Engineering at Oregon State University.

4.3 Data Processing

The raw data consists of a multitude of radiographs which are first corrected for distortion (distortion of the images is present due to the shape of the beam), and normalized for beam intensity fluctuations. The individual radiographs are then reconstructed into a three-dimensional volume.

Bentheimer sandstone contains pores and throats below the scanner resolution limit, resulting in partial volume effects. Ring artifacts and general noise produced by the x-ray CMT system also contribute artifacts to the reconstructed volume. Thus, segmentation of this data requires a more sophisticated method than simple grayscale histogram segmentation. A subsection (550^3 voxels) of the total volume is specified (generally containing the midpoint in the z-direction of the core) to be analyzed. This analytical cube is segmented using ROCK3DMA, which utilizes Indicator Kriging segmentation (Oh and Lindquist, 1999). Due to the relatively high level of noise and low resolution of the Bentheimer data, only two phases are identified in these volumes: NW phase vs. combined solid/W phase.

ROCK3DMA implements Indicator Kriging by identifying all pixels in the image which are below the lower threshold or above the upper threshold and labeling them as NW phase or rock/W phase respectively. For all pixels with grayscale values between the two thresholds, kriging is used to determine which phase to classify the pixels as. This process is shown for a 2-D slice in Figure 16 below. Each scan has a different amount of wetting fluid present, resulting in a different average attenuation for the volume and different scaling of grayscale values, so it was not possible to use a single set of threshold values for all scans. Instead, each scan is run through the program using multiple thresholds sets and the threshold set which provides the most accurate labeling is determined by visual inspection and used for further

analysis. Every threshold set is consistently separated by 1000 grayscale values.

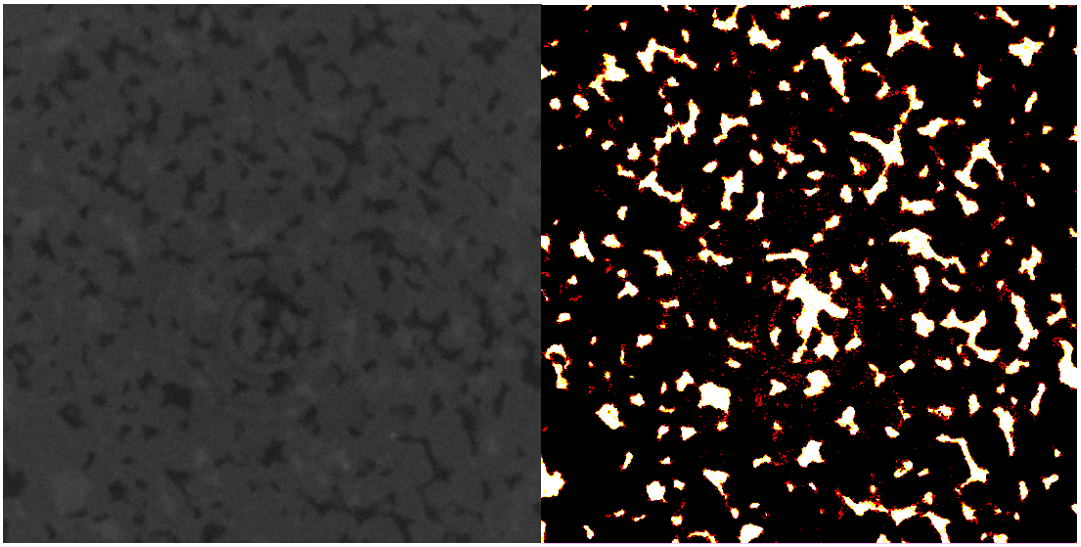

(a) (b)

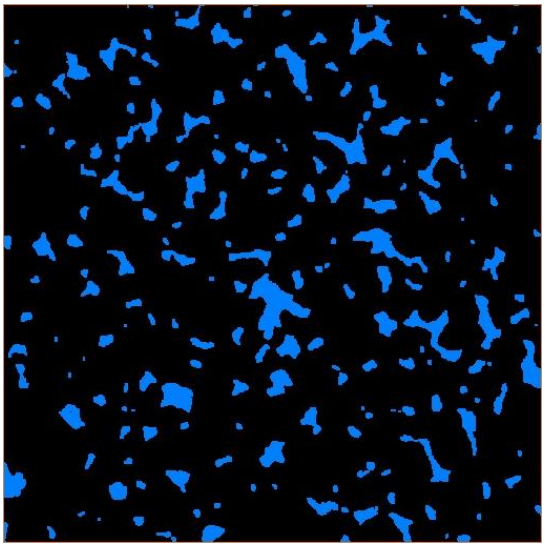

(c)

Figure 16. Segmentation by ROCK3DMA

(a) Grayscale image
(b) Results of indicator kriging: solid is automatically labeled black, NW fluid is automatically labeled white; red pixels are pixels between the threshold limits which have been determined to be solid, yellow pixels are pixels between the threshold limits which have been determined to be NW fluid
(c) Final segmented image

After segmentation, there are still a number of artificial falsely-labeled “NW phase blobs” present in the volume. A final cleanup algorithm is run using Avizo^{TM} which removes all blobs less than a volume of 100 voxels; this corresponds to a volume of 1,000,000 μm^3 (10×10^{-6} ml), or a cube with length of approximately 46 µm per side. This clean-up step removes less than 1% of the original NW saturation value.

At this point, Avizo^{TM} is used to quantify the amount of non-wetting phase present in each volume, calculate blob volumes and numbers, determine a composite Euler number for the volume, and create an isosurface of the NW fluid within the core.

4.4 REV Analysis

Due to the small sample sizes and the need to compare data from multiple rock cores, it was necessary to ensure that the data comprised a proper representative elementary volume (REV).

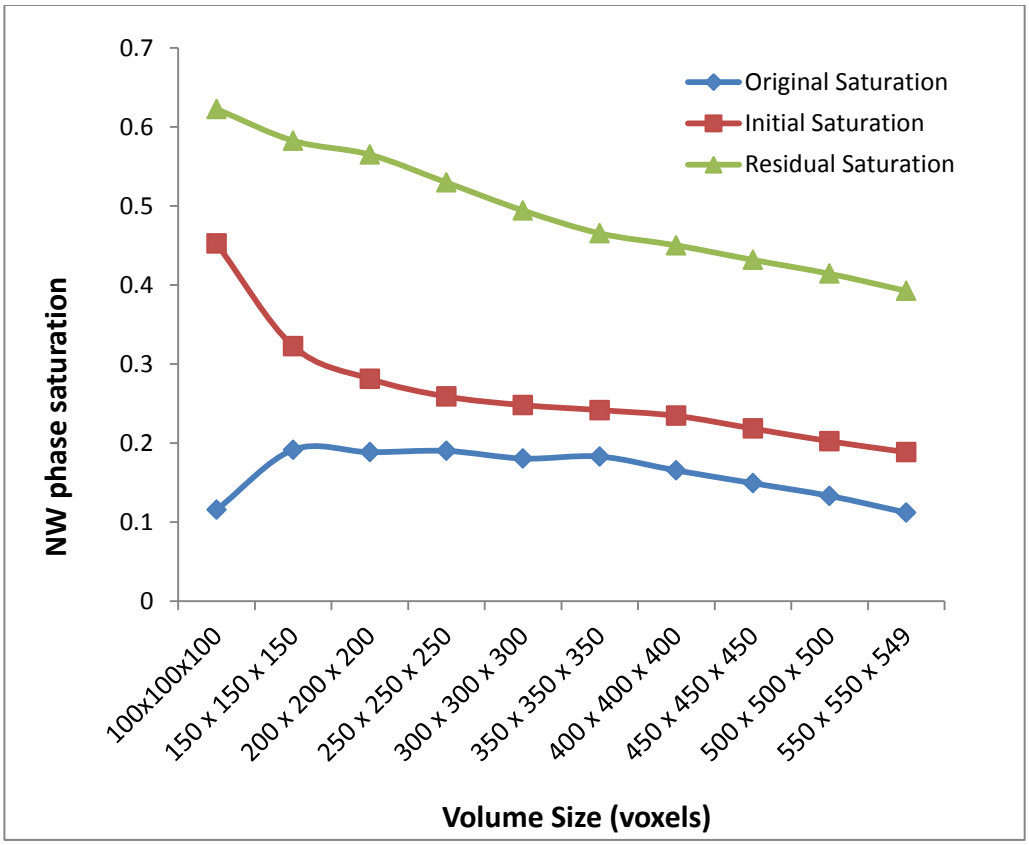

Figure 17. NW saturation as a function of analytical cube size

Figure 17 shows NW phase saturations as a function of analytical volume. There appears to be a plateau at intermediate sizes, followed by a consistent decrease in saturation above a threshold size value (e.g. approximately 350^3 voxels for the S_0 scan). The plateau demonstrates that sufficient size for a REV has been achieved. The decreasing trend implies that regions near the core walls may have impeded flow of NW fluid. Therefore, in order to ensure that a REV has been achieved while removing potential wall flow issues from analysis, cubes of 350 x 350 x 350 voxels were used for all quantitative analysis. As confirmation of this approach, Figure 18 shows the results of capillary number-saturation experiments as calculated from 350^3 voxel cubes

and 550^3 voxel cubes. As shown, the general trend is reproduced regardless of which size analytical cube is used.

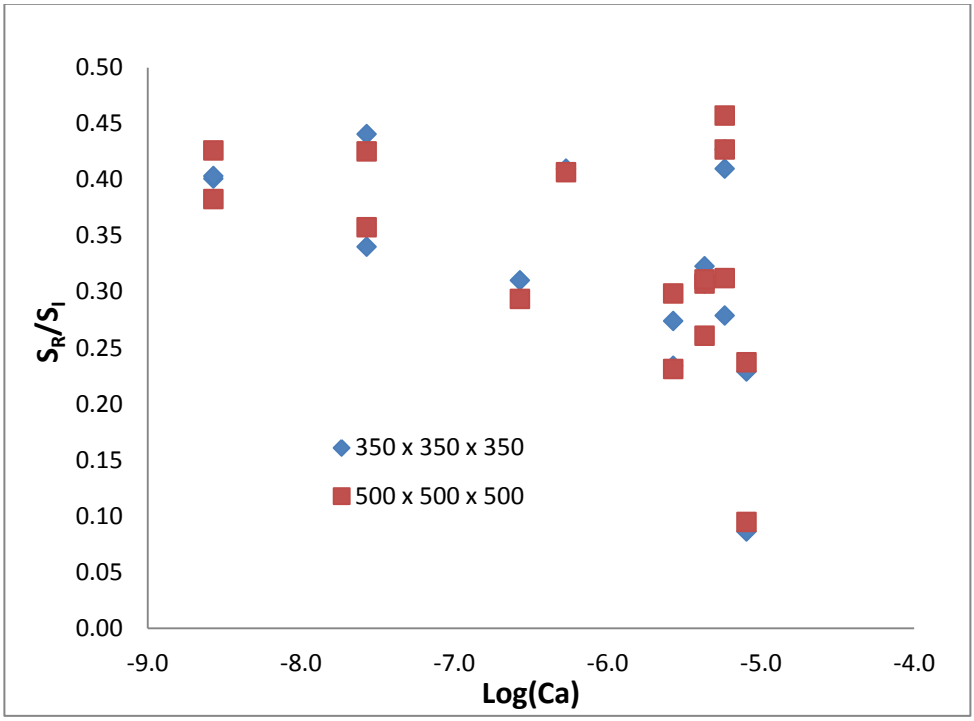

Figure 18. Comparison of 350^3 and 550^3 voxel analytical cube data

4.5 Glass Bead and Angular Sand Data

Section 5.3 below also includes data collected on glass bead cores and angular sand. These experiments were performed with similar fluid pairs, flow rates and experimental set-ups to the Bentheimer experiments described above. Glass bead data was collected with the same x-ray CMT system as used for Bentheimer experiments, but at a resolution of approximately 13 microns; full details can be found in Harper et al (2012). Anglular Sand data was collected at the Advanced Photon Source at Argonne National Lab at a resolution of 16.8 microns.

5.0 Results and Discussion

In this section, results will be discussed in terms of saturation, morphology, and topology of NW fluid.

5.1 Saturation and Capillary Number

Example isosurfaces from the experimental sequence for IFT =72, Ca = $10^{-5.1}$ and IFT=44.9, Ca = $10^{-5.4}$ are shown in Figure 19. Note that there is a significant amount of NW phase present in the S_0 scan, despite the W phase saturating measures taken as described above. The isosurfaces shown are for the same rock core; similarities in NW position due to pore structure are especially apparent in the S_0 and S_R scans. A scale bar is shown in the upper left image.

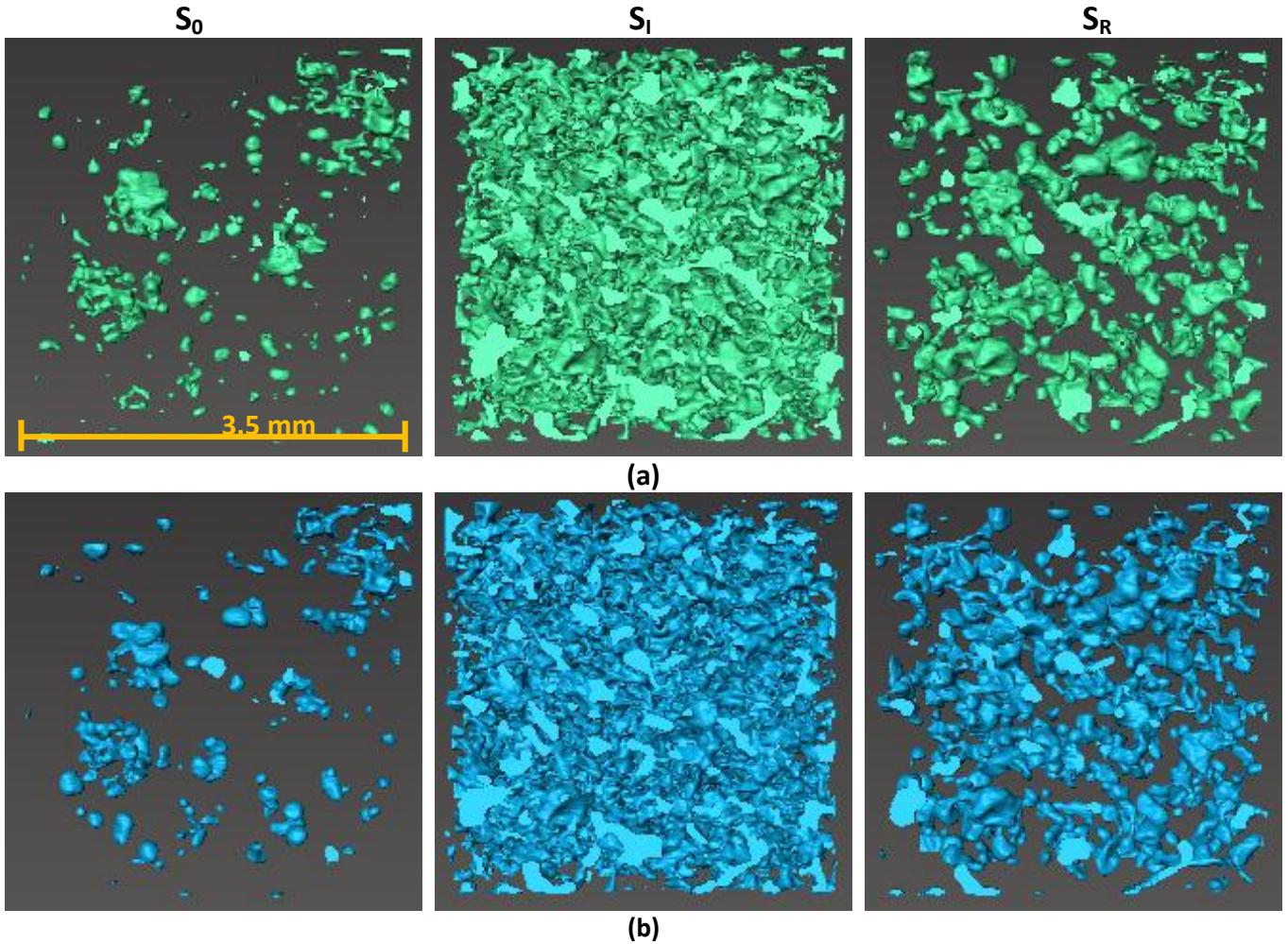

Figure 19. Example isosurfaces for S_0, S_I, and SR for rock core #10
(a) IFT=72, Ca = $10^{-5.1}$; (b) IFT= 44.9, Ca = $10^{-5.4}$

Figure 20 below shows the overall effect of flow rate and IFT variation on NW phase trapping. The results are shown collectively in the upper plot and individually in the lower plots for clarity, note the difference in scaling of the x-axis. Trapping here is shown as the residual saturation (after the final imbibition) normalized by the initial NW saturation (after drainage), S_R/S_I.

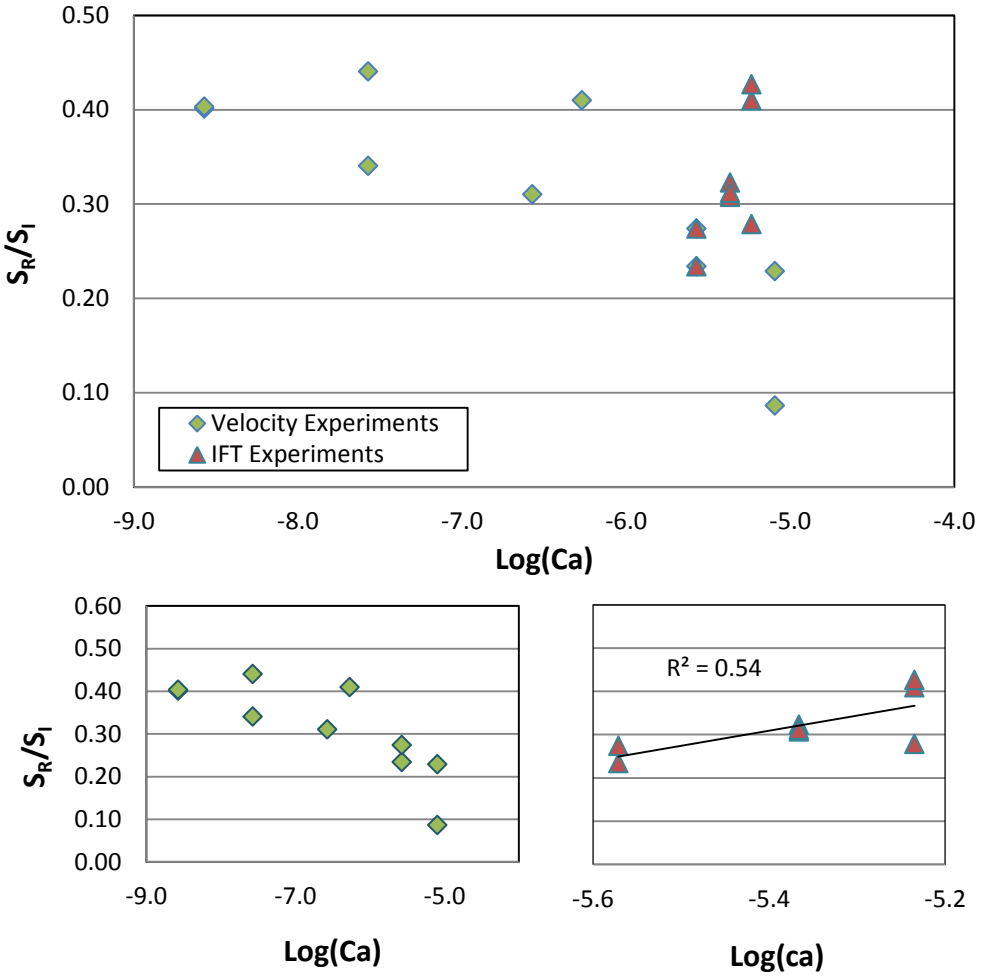

Figure 20. Effect of capillary number on NW phase trapping

In agreement with many previous studies on consolidated media, the overall trend of total NW phase trapping as a function of flow rate exhibits a general decrease as Ca increases beyond a critical value of approximately 10^{-6}.

Conversely, it appears that the influence of IFT on trapping shows the opposite trend: an increase in trapping as IFT increases. The maximum amount of residual NW phase was approximately 44% of the initial NW phase present in the Bentheimer, at Ca of $10^{-7.6}$

The relationship between residual NW saturation and fluid velocity shown in Figure 20 is in agreement with the relationships found by many other researchers in both experimental and model studies on consolidated medias (Suekane et al., 2010, Chatzis et al., 1988, Morrow et al., 1988, Hughes and Blunt, 2000, Nguyen et al., 2006). The reproduction of this trend here provides confirmation that the data collection and processing techniques used in this study are applicable and appropriate for this type of experiment. Differences in trapping efficiency between similar or same Ca number experiments will be examined further in section 5.3.

Experiments performed with varying IFT do not exhibit the expected trend as described above. There are multiple possible explanations for this result:

1. Magnitude of variation: flow velocities were varied by almost 5 orders of magnitude; however, it was only feasible to vary IFT by approximately a factor of two. Thus, it should be expected that flow velocity variation would have a more measurable effect on NW phase saturation than IFT modification (velocity experiments ranged from 9% to 44% trapping, IFT experiments ranged from 23% to 41%).
2. Initial NW Phase connectivity: this theory is examined further in section 5.3.

The effect of initial saturation on residual saturation was also investigated (Figure 21). Here, data from this work is overlaid on the plot presented by Al

Mansoori et al. (2009). While the data presented in this work does not exhibit a direct relation between initial and residual saturations, it does fall nicely within the general trapping trend observed by many others.

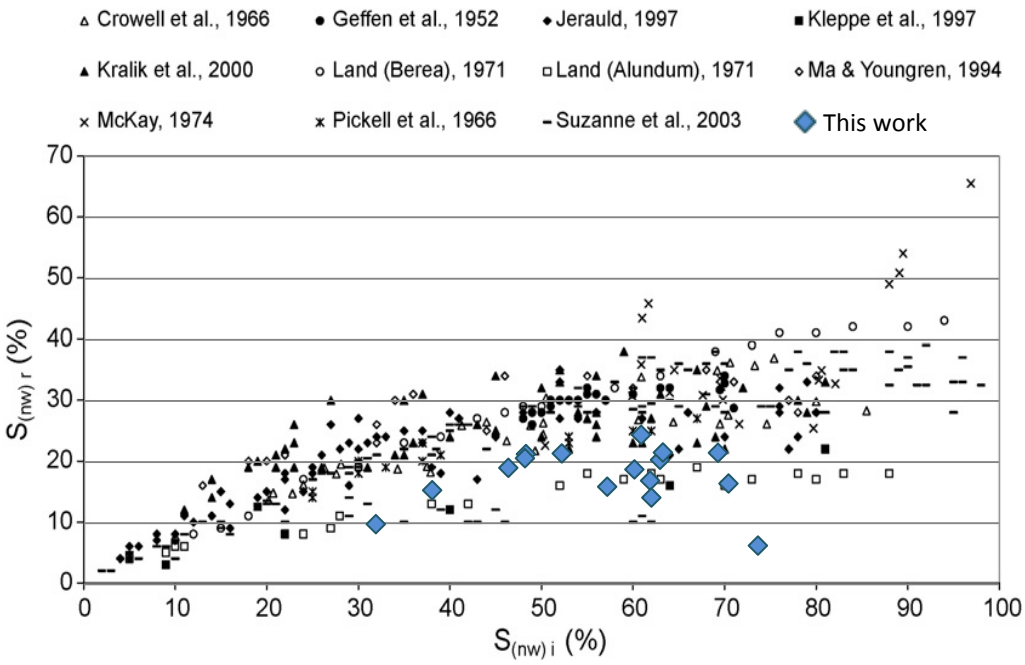

Figure 21. Residual saturation dependence on initial saturation (adapted from Al Mansoori et al, 2009)

5.2 NW Phase Morphology

Figure 22 demonstrates the impact of capillary number variation on residual NW phase morphology, quantified as average blob size and total normalized blob number. Normalized blob number indicates that the total number of blobs was divided by the corresponding NW saturation value for that scan. As shown, average blob volume decreases and normalized blob number increases as capillary number increases.

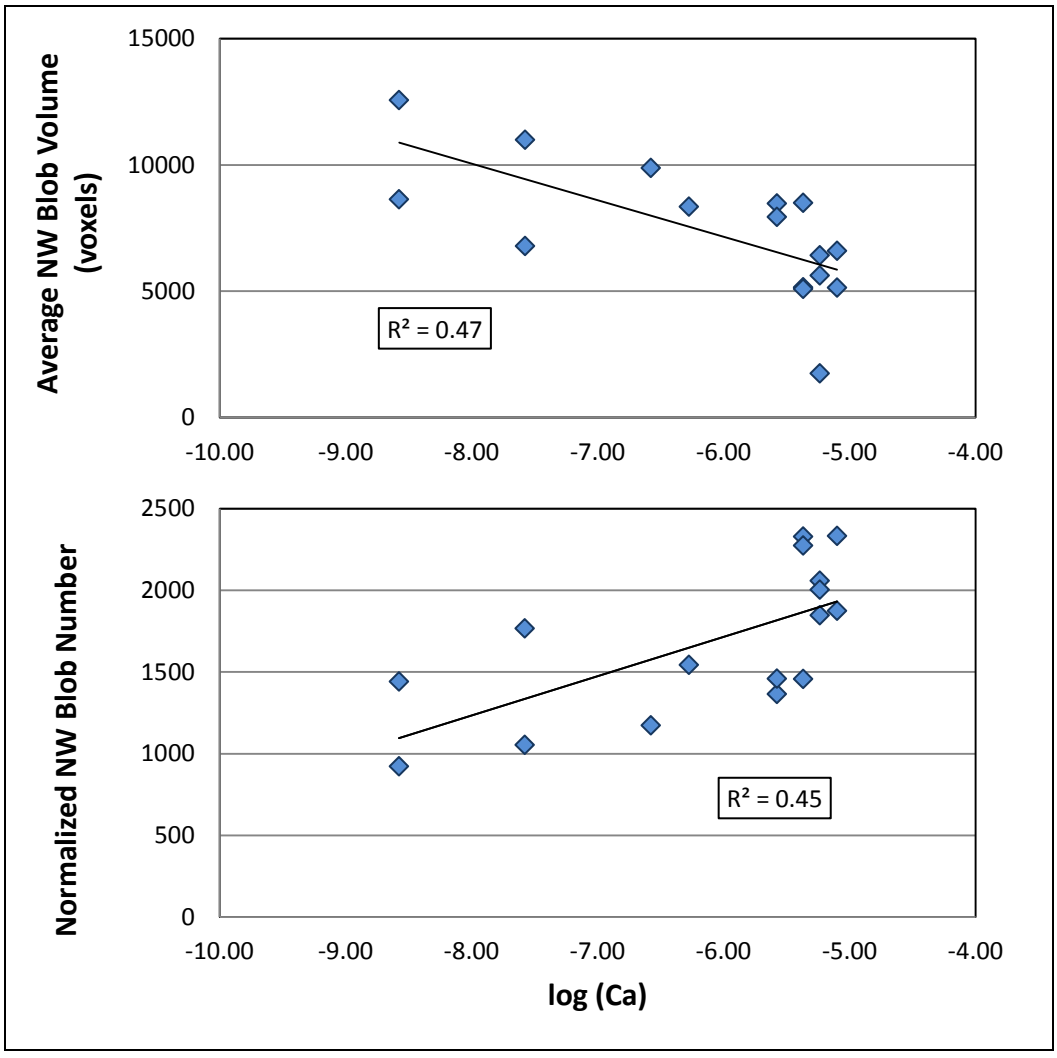

Figure 22. Influence of Ca on residual NW phase morphology

The individual effects of flow rate and IFT are shown separately in Figure 23.

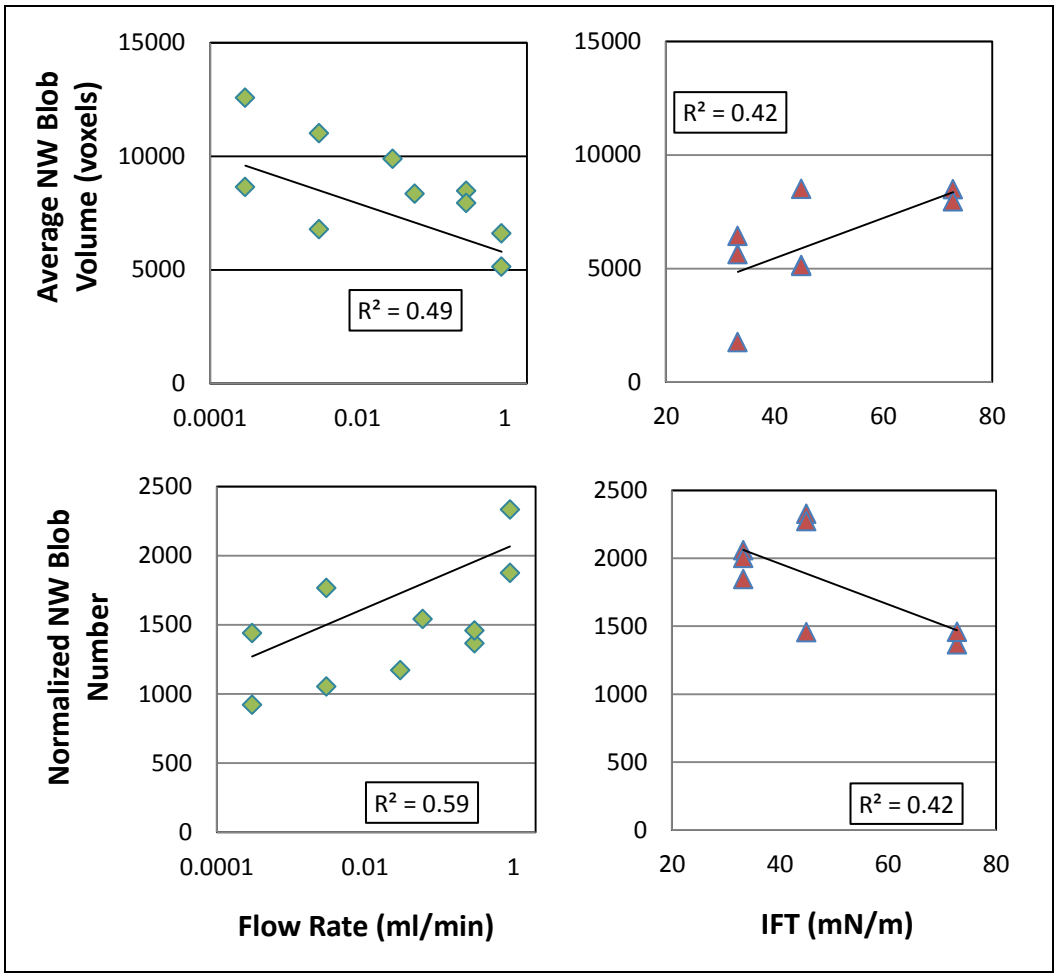

Figure 23. Effect of flow rate and IFT on residual NW phase morphology

As suggested by the illustrated relationship with Ca, average blob volume is inversely related to flow rate and positively correlated to IFT. Normalized blob number is positively correlated with flow rate and inversely related to IFT. Note that flow rates are shown on a logarithmic scale and IFT is shown on a linear scale for clarity.

Statistical significance of the correlation coefficients was checked using a t-distribution and Equation 11:

$$t = R\sqrt{\frac{n-2}{1-R^2}} \qquad (11)$$

where n is the number of samples and R^2 is the correlation coefficient. The results are shown in Table 4.

Table 4. Statistical significance of morphology trends of residual NW phase

Dependent Variable	Independent Variable	n	d.f.	R^2	t-value	Two sided p-value
Blob Volume	Log(Ca)	16	14	0.47	3.524	0.003
Normalized Blob Number	Log(Ca)	16	14	0.45	3.384	0.004
Blob Volume	Flow Rate	10	8	0.49	2.772	0.024
Normalized Blob Number	Flow Rate	10	8	0.59	3.393	0.009
Blob Volume	IFT	8	6	0.42	2.407	0.043
Normalized Blob Number	IFT	8	6	0.42	2.407	0.043

As shown in Table 4, there is strong evidence (p-value <0.05) that the overall Ca number is correlated with morphology. Additionally, there is strong evidence that both flow rate and IFT are individually correlated with average blob volume and normalized blob number.

While flow rate was only changed during the final imbibition process (S_R), IFT affects the entire experiment cycle, including the initial primary imbibition (S_0) and the primary drainage (S_I). Figure 24 shows average blob volume and blob number over the range of saturation values achieved in experiments as a function of IFT. Note that because these relationships are shown versus saturation, the total blob number is used instead of the normalized blob number.

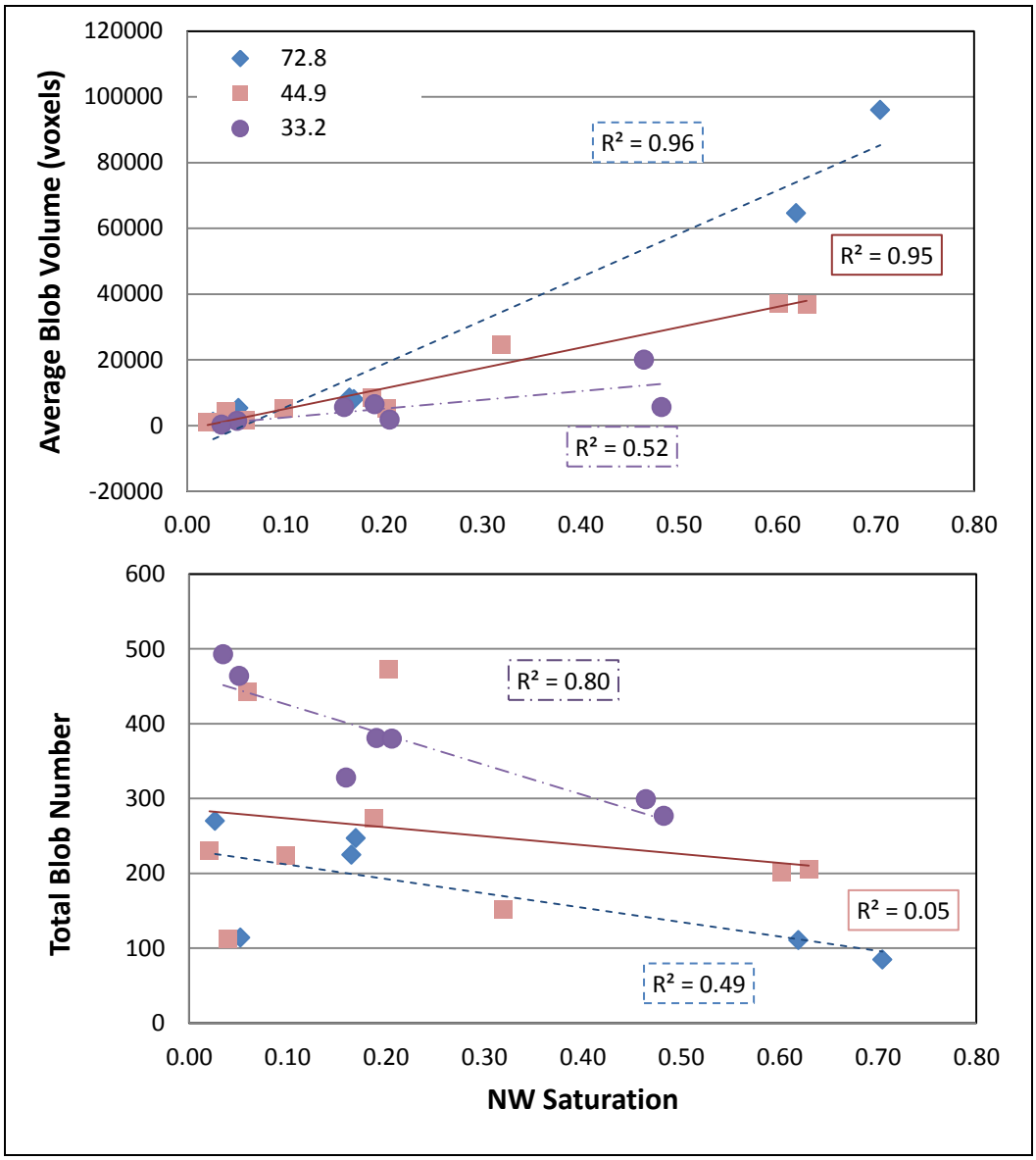

Figure 24. Impact of IFT (in mN/m) on NW phase morphology for all experimental stages

As saturation increases the average blob volume increases and the total blob number decreases. This is due to the coalescence of smaller blobs as the pore space fills with NW fluid. Again, the trends of average blob volume appear to be correlated to IFT; however, the relationship between blob number and IFT

is less clear. A summary of the statistics associated with these trendlines is presented in Table 5.

Table 5. Statistical significance of IFT-morphology trend for all NW phase

IFT (mN/m)	n	d.f.	R^2	t-value	Two sided p-value
Blob Volume					
72.8	6	4	0.96	9.798	<0.001
44.9	9	7	0.95	11.533	<<0.001
33.2	9	7	0.52	2.754	0.028
Blob Number					
72.8	6	4	0.49	2.192	0.093
44.9	9	7	0.05	0.607	0.563
33.2	9	7	0.80	5.292	0.001

Table 5 shows that while the average blob volume-IFT relationships are strongly statistically significant, blob number-IFT relationships vary in significance. Note also from Figure 24 that the difference in average blob volumes is amplified at higher NW saturation values.

The trends shown in Figures 22 and 23 indicate that fluid velocity and IFT have the expected effect on blob size, i.e. an increase in capillary number (increasing velocity and/or decreasing IFT) leads to a decrease in average blob volume. Indeed, Figure 24 shows that decreasing IFT has the effect of decreasing blob size over the entire course of the experimental process. These results are supported by the work of Chatzis et al. (1988) and Chao et al. (2000).

It is intuitively discernible that for a given saturation value, as average blob volume decreases, the total blob number must increase; this assumption is confirmed for residual blob numbers by Figure 22 and 23. However, Figure 24

demonstrates that the blob number-IFT relationship is statistically insignificant when considered over the entire experimental process.

This blob number inconsistency is possibly a result of data processing measures: due to the presence of noise and the relatively low resolution of the data obtained in this experiment, all NW phase blobs of size less than 100 voxels were removed (see Section 4.3). It is possible than some of the fluid elements that were removed were actual physical NW fluid blobs rather than noise; and although removing these small elements has a negligible impact on overall saturation, it may have distorted the morphological measurements. This problem would become more severe as blob size distributions shift towards smaller blobs.

Despite this issue, the overall trends indicate that an increase in capillary number results in a decrease in average NW blob volume and an increase in the number of blobs. Smaller blob volume indicates that dissolution would be enhanced; however, as discussed above, high capillary number imbibition generally results in reduced total residual saturation. The trade-off between NW saturation and morphology should be considered when designing a CO_2 sequestration scenario.

5.3 NW Phase Topology

The connectivity of NW phase throughout the experimental sequence is demonstrated via use of the Euler number as shown in Figure 25. Positive Euler numbers indicate NW phase exists as disconnected, isolated blobs; negative values of Euler numbers indicate more connected, complex NW blob structure. As shown, after primary imbibition (S_0) the original NW phase exists in positive Euler space; after drainage (S_I), the initial NW phase is highly connected and the corresponding Euler numbers are negative; and after

secondary imbibition (S_R), the residual NW phase is again disconnected with positive Euler numbers. This confirms that the NW blobs present in the residual scans are indeed trapped and isolated.

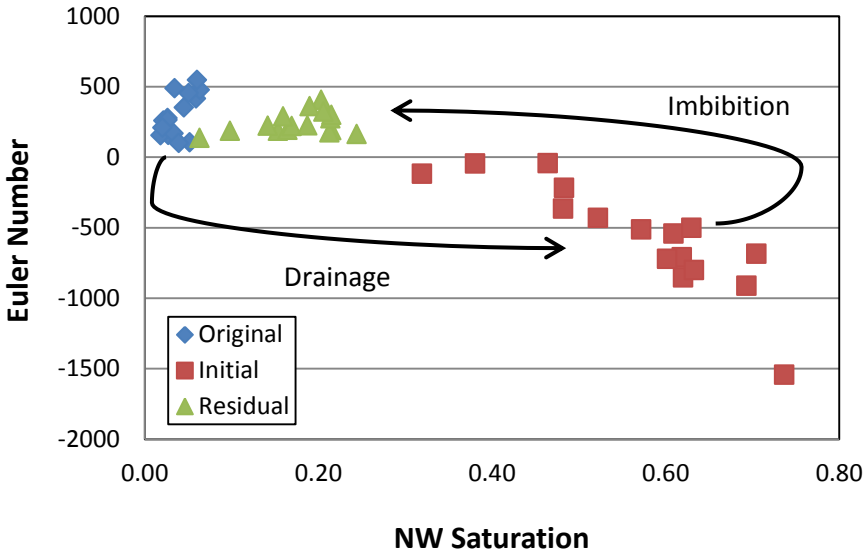

Figure 25. Connectivity of NW phase over experimental sequence

It has been suggested that the topology of NW phase after drainage can influence the trapped NW after secondary imbibition (Wardlaw and Yu, 1988). This was investigated by plotting trapped NW phase as a function of initial NW phase Euler number (Figure 26).

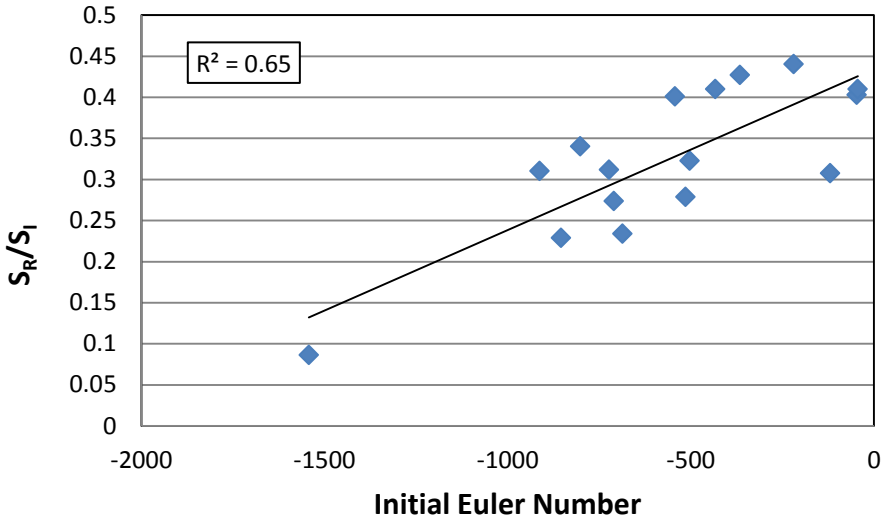

Figure 26. Dependence of trapping on initial NW phase topology

The statistics associated with this relationship are shown in Table 6.

Table 6. Statistical Significance of the Euler-residual trapping relationship

n	d.f.	R^2	t-value	Two sided p-value
16	14	0.65	5.099	>0.001

The low p-value reported here indicates that there is a strong correlation between the initial connectivity of NW phase and residual trapping. To explore this further, we revisit the capillary number- saturation relationships shown in Section 5.1. In the velocity experiments, there were three sets of data points which demonstrate notably different trapping values despite being performed at the same or similar capillary number values. These data points have been labeled with their initial NW phase Euler number value in Figure 27. Note that the points with more well-connected initial NW phase (more negative Euler number values) exhibit significantly lower trapping values.

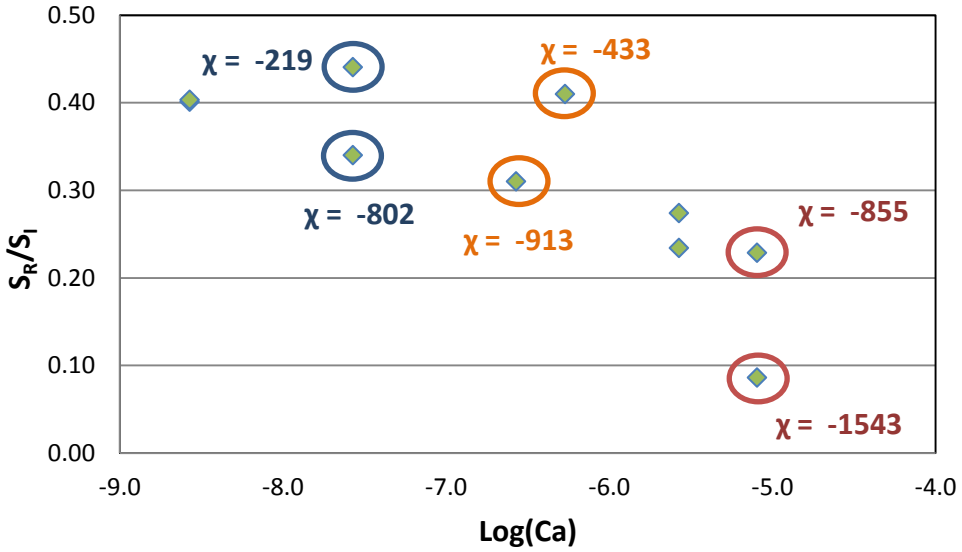

Figure 27. Influence of initial Euler number on velocity-trapping relationship

Similarly, the trend of increased trapping with increasing IFT shown earlier (Figure 20, reproduced in Figure 28) may be influenced by the initial Euler number: Figure 28 presents the trapped NW phase as a function of Ca as compared to the range of initial NW phase Euler numbers for each IFT grouping. Error bars on the Euler numbers represent one standard deviation of Euler Number values for each IFT group.

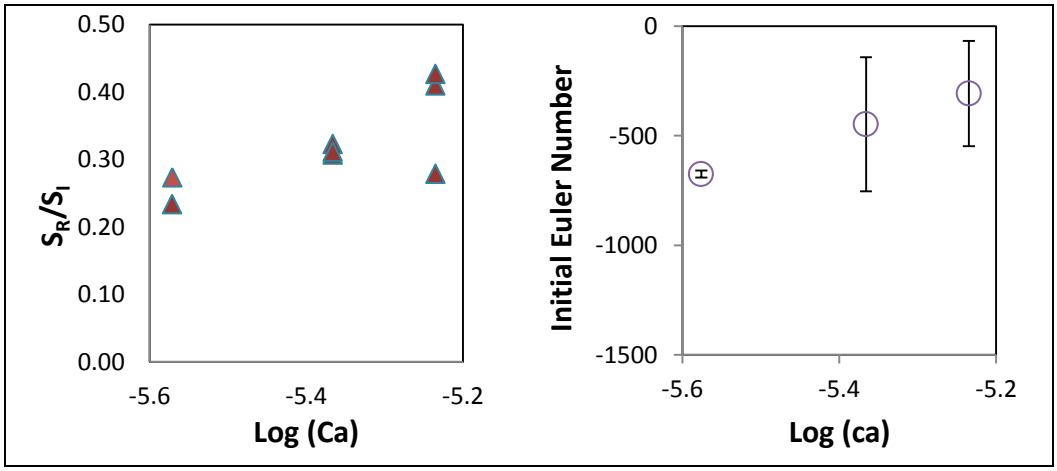

Figure 28. Influence of initial Euler number on IFT-trapping relationship

The low S_l connectivity (less negative Euler numbers) at low IFT is possibly due to the method of saturation control in these experiments; i.e. instead of imposing an external pressure gradient and allowing the saturation to equilibrate, we pump a certain volume and allow pressure to equilibrate to the change in saturation. Despite considerable effort to remove air bubbles from flow lines, small bubbles are generally present in fluid lines or attached to the interior of valves. Thus, the volume pumped by the syringe pump may not correspond exactly to the volume pumped into/out of the core as bubbles expand or contract due to the pressure change, and these discrepancies in pumped volume could have significant effects on connectivity, as examined further in Figure 29. Any bubble issues present in the experimental system would be intensified as IFT decreases. Even in the absence of bubbles, IFT may have an independent impact on NW phase connectivity after drainage; this study does not provide enough data to draw any conclusions on this theory. The effect of IFT on the initial phase connectivity should be studied in more detail as this may contribute to an advantageous trapping strategy.

NW phase topology as a function of saturation was investigated for different media. Figure 29 shows the results for Bentheimer sandstone, glass beads, and angular sand. Results are normalized to physical media volume to allow for a valid comparison between different samples. NW fluid exhibits more extreme connectivity values at low and high saturation values in Bentheimer sandstone as compared to either of the unconsolidated media. Angular sand maintains very low connectivity even at a NW saturation of 100%. The glass bead system lies between these two curves. These trends may be related to grain size or consolidated vs. unconsolidated media type, but further analysis of media properties is needed to understand the complete context of this behavior.

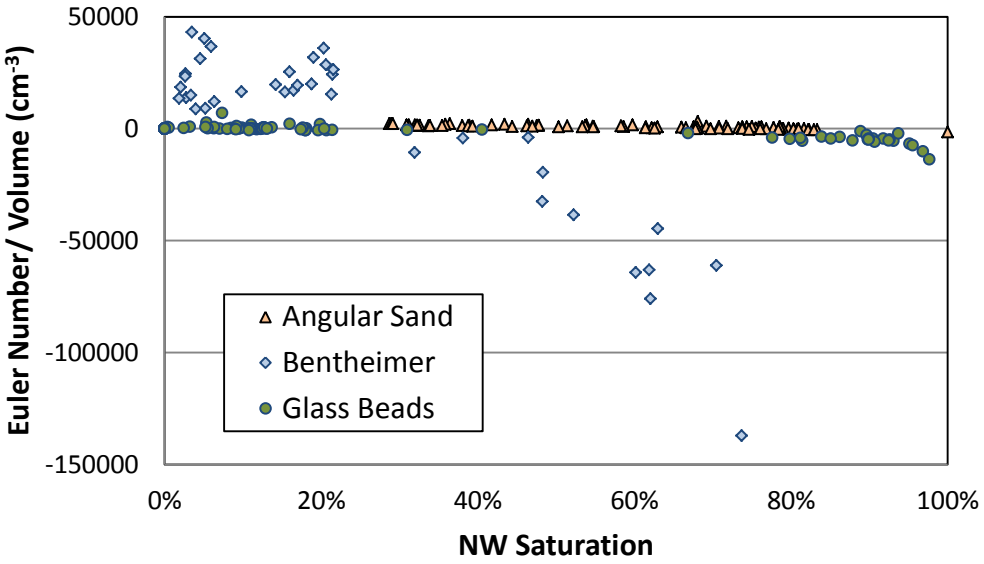

Figure 29. Connectivity of various media as a function of NW phase saturation

Taken all together, these results suggest that topological characterization of NW fluid within a specific reservoir medium is crucial for successful utilization of capillary trapping.

For example, if the medium allows NW phase connectivity at low saturation (e.g. Bentheimer sandstone), a water-alternating-gas (WAG) scheme might enhance CO_2 trapping, since this method breaks up the continuous CO_2 plume into smaller, more discrete fluid packets and would discourage a continuous initial NW phase. However, a WAG scheme also requires injection of water at velocities which could exceed the threshold capillary number for mobilization of residual NW phase. For a system which exhibits low connectivity even at high NW saturation (e.g. unconsolidated angular sand), this technique would likely reduce, rather than enhance, overall trapping. Thus, it is important to

use both the Ca-saturation and the Euler number-saturation relationships to determine an optimal injection strategy for a given medium.

6.0 Conclusion

This work examined the impact of a viscosity force parameter, fluid velocity, and a capillary force parameter, interfacial tension, on the saturation, morphology, and topology of NW fluid (air, used as a proxy for supercritical CO_2) in a Bentheimer sandstone after primary imbibition, drainage, and secondary imbibition. Experiments were quantified via x-ray CMT, which allows for three dimensional, non-destructive, pore-scale analysis of the amount and distribution of NW phase fluid within the sandstone cores. The main research findings are summarized here:

6.1 Saturation

- Trapped NW phase saturation decreases with increases in fluid velocity.
- Trapped NW phase saturation increases with decreases in IFT (this finding is subject to other concerns, i.e. initial phase connectivity).
- The overall Ca-saturation trend indicates that trapped NW phase will decrease above a critical capillary number of approximately 10^{-6}.

6.2 Morphology

- Residual average NW blob volume decreases with increases in Ca.
- Residual NW blob number increases with increases in Ca.
- Average NW blob volume increases as IFT increases for all stages of the imbibition-drainage-imbibition experimental cycle.

6.3 Topology

- The Euler number can be used as a metric to determine if residual NW phase is connected or trapped.
- NW phase trapping is dependent on initial NW phase connectivity within the porous medium, with lower values of Euler number resulting in less trapping.

6.4 Relevance to Capillary Trapping of Supercritical CO_2

The saturation results indicate that the previously recognized relationship between Ca and NW phase trapping can be assumed for a CO_2-brine system, with the caveat that the role of IFT does not follow expected trends, and the influence of IFT on initial phase connectivity should be investigated more thoroughly. Morphological findings show the expected result that average blob volumes are inversely related to Ca and blob numbers are positively correlated to Ca. This indicates that in order to enhance dissolution processes, high-Ca brine imbibition should follow a CO_2 injection; however, this scenario may also result in the mobilization of trapped CO_2 blobs and decreased total residual CO_2 saturation. Thus, care must be taken to determine optimal sequence of injection parameters in order to balance these two concerns. Finally, the initial NW phase connectivity should be considered when designing a sequestration scheme, as highly connected initial NW phase results in lower residual saturations. This indicates that a WAG scheme may be advantageous for certain media types, as the intermittent brine injections may break up the connected CO_2 phase and decrease overall NW connectivity. The Ca-saturation, Ca-morphology, and Euler number-saturation relationships should all be considered in order to optimize capillary trapping during a CO_2 sequestration scenario.

Bibliography

AL-RAOUSH, R. I. & WILLSON, C. S. 2005. A pore-scale investigation of a multiphase porous media system. *Journal of Contaminant Hydrology,* 77**,** 67-89.

AL MANSOORI, S., IGLAUER, S., PENTLAND, C. H., BIJELJIC, B. & BLUNT, M. J. 2009. Measurements of Non-Wetting Phase Trapping Applied to Carbon Dioxide Storage. *Energy Procedia,* 1**,** 3173-3180.

ARNS, J. Y., ROBINS, V., SHEPPARD, A. P., SOK, R. M., PINCZEWSKI, W. & KNACKSTEDT, M. A. 2004. Effect of network topology on relative permeability. *Transport in Porous Media,* 55**,** 21-46.

BACHU, S. 2003. Screening and ranking of sedimentary basins for sequestration of CO2 in geological media in response to climate change. *Environmental Geology,* 44**,** 277-289.

BACHU, S. & BENNION, B. 2008. Effects of in-situ conditions on relative permeability characteristics of CO_2-brine systems. *Environmental Geology,* 54**,** 1707-1722.

BLUNT, M. J., BIJELJIC, B., DONG, H., GHARBI, O., IGLAUER, S., MOSTAGHIMI, P., PALUSZNY, A. & PENTLAND, C. 2012. Pore-scale imaging and modelling. *Advances in Water Resources*.

CENSE, A. W. & BERG, S. Year. The Viscous-Capillary Paradox in 2-Phase Flow in Porous Media. *In:* International Symposium of the Society of Core Analysts, 27-30 September, 2009 2009 Noordwijk, The Netherlands. Shell International Exploration & Production.

CHAO, W.-L., PARLANGE, J. Y. & STEENHUIS, T. S. 2000. An Analysis of the Movement of Wetting and Nonwetting Fluids in Homogeneous Porous Media. *Transport in Porous Media,* 41**,** 121-135.

CHATZIS, I., KUNTAMUKKULA, M. S. & MORROW, N. R. 1988. Effect of capillary number on the microstructure of residual oil in strongly water-wet sandstones. *Journal Name: SPE (Society of Petroleum Engineers) Reserv. Eng.; (United States); Journal Volume: 3:3***,** Medium: X; Size: Pages: 902-912.

CHATZIS, I., MORROW, N. & LIM, H. 1983. Magnitude and detailed structure of residual oil saturation. *Old SPE Journal,* 23**,** 311-326.

CHATZIS, I. & MORROW, N. R. 1984. Correlation of capillary number relationships for sandstone. *Journal Name: SPEJ, Soc. Pet. Eng. J.; (United States); Journal Volume: 24:5***,** Medium: X; Size: Pages: 555-562.

DING, M. & KANTZAS, A. 2007. *Capillary number correlations for gas-liquid systems,* Calgary, CANADA, Society of Petroleum Engineers.

GITTINS, P., IGLAUER, S., PENTLAND, C. H., AL-MANSOORI, S., AL-SAYARI, S., BIJELJIC, B. & BLUNT, M. J. 2010. Nonwetting phase residual saturation in sand packs. *Journal of Porous Media,* 13**,** 591-599.

HARPER, E. J., D. WILDENSCHILD, R.T. ARMSTRONG, A.L. HERRING, AND B.K. BAY 2012. Optimization of capillary trapping in unconsolidated porous media. *submitted to Transport in Porous Media*.

HATIBOGLU, C. U. & BABADAGLI, T. 2010. Experimental and visual analysis of co- and counter-current spontaneous imbibition for different viscosity ratios, interfacial tensions, and wettabilities. *Journal of Petroleum Science and Engineering,* 70**,** 214-228.

HEIß, V., NEUWEILER, I., OCHS, S. & FÄRBER, A. 2011. Experimental investigation on front morphology for two-phase flow in heterogeneous porous media. *Water Resources Research,* 47**,** W10528.

HUGHES, R. G. & BLUNT, M. J. 2000. Pore Scale Modeling of Rate Effects in Imbibition. *Transport in Porous Media,* 40**,** 295-322.

IPCC 2005. *IPCC special report on carbon dioxide capture and storage*.

KETCHAM, R. A. & CARLSON, W. D. 2001. Acquisition, optimization and interpretation of X-ray computed tomographic imagery: applications to the geosciences. *Computers & Geosciences,* 27**,** 381-400.

LENORMAND, R., TOUBOUL, E. & ZARCONE, C. 1988. Numerical models and experiments on immiscible displacements in porous media. *Journal of Fluid Mechanics,* 189**,** 165-187.

MAHMUD, W. M., ARNS, J. Y., SHEPPARD, A., KNACKSTEDT, M. A. & PINCZEWSKI, W. V. 2007. Effect of network topology on two-phase imbibition relative permeability. *Transport in Porous Media,* 66**,** 481-493.

MAYER, A. S. & MILLER, C. T. 1992. The influence of porous medium characteristics and measurement scale on pore-scale distributions of residual nonaqueous-phase liquids. *Journal of Contaminant Hydrology,* 11**,** 189-213.

MAYER, A. S. & MILLER, C. T. 1993. An experimental investigation of pore-scale distributions of nonaqueous phase liquids at residual saturation. *Transport in Porous Media,* 10**,** 57-80.

MORROW, N. R., CHATZIS, I. & TABER, J. T. 1988. Entrapment and mobilization of residual oil in bead packs. *Journal Name: SPE (Society of Petroleum Engineers) Reserv. Eng.; (United States); Journal Volume: 3:3***,** Medium: X; Size: Pages: 927-934.

NGUYEN, V. H., SHEPPARD, A. P., KNACKSTEDT, M. A. & VAL PINCZEWSKI, W. 2006. The effect of displacement rate on imbibition relative permeability and residual saturation. *Journal of Petroleum Science and Engineering,* 52**,** 54-70.

OH, W. & LINDQUIST, B. 1999. Image thresholding by indicator kriging. *Pattern Analysis and Machine Intelligence, IEEE Transactions on,* 21**,** 590-602.

POLAK, S., CINAR, Y., HOLT, T. & TORSÆTER, O. 2011. An experimental investigation of the balance between capillary, viscous, and gravitational forces during CO2 injection into saline aquifers. *Energy Procedia,* 4**,** 4395-4402.

SCHECHTER, D., ZHOU, D. & ORR, F. 1994. Low IFT drainage and imbibition. *Journal of Petroleum Science and Engineering,* 11**,** 283-300.

SCHRAG, D. P. 2007. Preparing to Capture Carbon. *Science,* 315**,** 812-813.

SETIAWAN, A., NOMURA, H. & SUEKANE, T. 2012. Microtomography of Imbibition Phenomena and Trapping Mechanism. *Transport in Porous Media,* 92**,** 243-257.

SHEN, P., ZHU, B., LI, X.-B. & WU, Y.-S. 2010. An Experimental Study of the Influence of Interfacial Tension on Water–Oil Two-Phase Relative Permeability. *Transport in Porous Media,* 85**,** 505-520.

SILIN, D., TOMUTSA, L., BENSON, S. & PATZEK, T. 2011. Microtomography and Pore-Scale Modeling of Two-Phase Fluid Distribution. *Transport in Porous Media,* 86**,** 495-515.

SOK, R. M., KNACKSTEDT, M. A., SHEPPARD, A. P., PINCZEWSKI, W., LINDQUIST, W., VENKATARANGAN, A. & PATERSON, L. 2002. Direct and stochastic generation of network models from tomographic images; effect of topology on residual saturations. *Transport in Porous Media,* 46**,** 345-371.

SUEKANE, T., ZHOU, N., HOSOKAWA, T. & MATSUMOTO, T. 2010. Direct Observation of Trapped Gas Bubbles by Capillarity in Sandy Porous Media. *Transport in Porous Media,* 82**,** 111-122.

VAN GEEL, P. J. & ROY, S. D. 2002. A proposed model to include a residual NAPL saturation in a hysteretic capillary pressure–saturation relationship. *Journal of Contaminant Hydrology,* 58**,** 79-110.

VIZIKA, O., AVRAAM, D. G. & PAYATAKES, A. C. 1994. On the role of the viscosity ratio during low-capillary-number forced imbibition in porous media. *Journal Name: Journal of Colloid and Interface Science; (United States); Journal Volume: 165:2***,** Medium: X; Size: Pages: 386-401.

VOGEL, H. J. 2002. Topological characterization of porous media. *Morphology of Condensed Matter***,** 75-92.

VOGEL, H. J., WELLER, U. & SCHLÜTER, S. 2010. Quantification of soil structure based on Minkowski functions. *Computers & Geosciences,* 36**,** 1236-1245.

WANG, Y., ZHANG, C., WEI, N., OOSTROM, M., WIETSMA, T. W., LI, X. & BONNEVILLE, A. 2012. Experimental Study of Crossover from Capillary to Viscous Fingering for Supercritical CO2–Water Displacement in a Homogeneous Pore Network. *Environmental Science & Technology*.

WARDLAW, N. C. 1986. Mechanisms of nonwetting phase trapping during imbibition at slow rates. *Journal of colloid and interface science,* 109**,** 473-486.

WARDLAW, N. C. & YU, L. 1988. Fluid topology, pore size and aspect ratio during imbibition. *Transport in Porous Media,* 3**,** 17-34.

WILDENSCHILD, D. & SHEPPARD, A. P. 2012. X-ray imaging and analysis techniques for quantifying pore-scale structure and processes in subsurface porous medium systems. *Advances in Water Resources*.

WILDENSCHILD, D., VAZ, C. M. P., RIVERS, M. L., RIKARD, D. & CHRISTENSEN, B. S. B. 2002. Using X-ray computed tomography in hydrology: systems, resolutions, and limitations. *Journal of Hydrology,* 267**,** 285-297.

YADALI JAMALOEI, B., ASGHARI, K. & KHARRAT, R. 2012. The investigation of suitability of different capillary number definitions for flow behavior characterization of surfactant-based chemical flooding in heavy oil reservoirs. *Journal of Petroleum Science and Engineering,* 90–91**,** 48-55.

YOUSSEF, S., BAUER, D., BEKRI, S., ROSENBERG, E. & VIZIKA-KAVVADIAS, O. Year. 3D In-Situ Fluid Distribution Imaging at the Pore Scale as a New Tool For Multiphase Flow Studies. *In:* SPE Annual Technical Conference and Exhibition, 2010.